

# Equivalent layer technique: an extended review and new contributions

Vanderlei C. Oliveira Jr.<sup>1</sup> and Valéria C. F. Barbosa<sup>1</sup>

<sup>1</sup> *Observatório Nacional, Rio de Janeiro, Brazil*

*e-mails: vandscoelho@gmail.com, valcris@on.br*

(September 23, 2016)

**GEO-2015-XXXX**

Running head: **Equivalent layer technique**

## ABSTRACT

Equivalent layer technique is a powerful tool for processing gravity and magnetic data (e.g., interpolation, reduction to the pole, upward and downward continuations). Grounded on well-established concepts of potential theory, this technique allows that a discrete set of observations of a potential field produced by arbitrary sources can be exactly reproduced by a fictitious 2D physical-property distribution which is defined on a surface located below the observations. This technique takes advantage of the inherent ambiguity of determining the true physical-property distribution producing a given potential field. Mathematically, it consists in approximating a discrete set of potential-field observations by a linear combination of harmonic functions. These harmonic functions, in turn, represent the potential field produced by a fictitious physical-property distribution defined on a layer. This fictitious layer, called equivalent layer, is then posteriorly used to compute transformations of the observed potential-field data. We present a in-depth review of the mathematical

foundations and physical meaning of the equivalent layer technique, in both continuous and discrete cases, by considering both planar and undulating equivalent layers. We show that the magnetic-moment distribution within a planar equivalent layer of dipoles must have the same constant magnetization direction of the magnetic sources for the purpose of correctly reducing the total-field anomaly to the pole. We prove that, in this case, the magnetic-moment distribution is all-positive even if the magnetization intensity varies within the sources. Moreover, we review the computation aspects of the equivalent technique and show how previous works have been dealt with its high computational cost. We present several tests with synthetic data showing not only theoretical aspects, but also the powerful flexibility of the equivalent layer in processing potential-field data.

## INTRODUCTION

Equivalent layer technique appeared in the geophysical literature over 50 years ago and have been used as a versatile tool to process potential-field data. This technique can be used to compute different data processing such as interpolation (e.g., Cordell, 1992; Mendonça and Silva, 1994; Barnes, 2012), upward (or downward) continuation (e.g., Emilia, 1973; Hansen and Miyazaki, 1984; Li and Oldenburg, 2010) reduction to the pole of magnetic data (e.g., Silva, 1986; Leão and Silva, 1989; Guspí and Novara, 2009; Oliveira Jr. et al., 2013), gradient data processing (Barnes and Lumley, 2011), satellite-data processing (Mayhew, 1982), computing geoid undulations (Guspí et al., 2004), merging multiple datasets (Boggs and Dransfield, 2004; Lane, 2004) and de-noising gradient data (Martinez and Li, 2016).

The seminal paper presented by Siméon Denis Poisson to the French Academy of Sciences in 1824 contains the first ideas about the equivalent layer technique. In his work, Poisson showed that the magnetic intensity produced outside a given magnetic body is the same as would be produced by a combination of two fictitious magnetization distributions, one defined over the surface and another defined throughout the volume of the magnetic body. These fictitious magnetization distributions are generally known as Poisson’s equivalent surface- and volume-distributions of magnetism (Whittaker, 2012). Some years later, the Poisson’s investigations were generalized and extended by George Green in his ground-breaking paper *An essay on the application of mathematical analysis to the theories of electricity and magnetism, Nottingham, 1828*. Green, who was the first to use the term “potential”, followed a mathematical approach that had already been used by Lagrange, Laplace, and Poisson to present a formula generalizing the Poisson’s result on the equivalent surface- and volume-distributions of magnetism. By using this formula, which is

now commonly called Green's Theorem, Green deduced many results of remarkable beauty and interest in potential theory (Kellogg, 1929; Whittaker, 2012).

The equivalent layer technique is grounded on potential theory, which is the theory of the Laplace's differential equation. Mathematically, a solution of Laplace's equation is called a harmonic function. A function  $U(x, y, z)$  at a point  $(x, y, z)$  is harmonic if its second derivatives exist, are continuous, and satisfy Laplace's equation throughout some neighbourhood of that point. A well-known tool for deriving and understanding properties of harmonic functions is a set of Green's identities (Kellogg, 1929). In accordance with potential theory, a discrete set of observations of a potential field produced by arbitrary sources can be exactly reproduced by a continuous and infinite 2D physical-property distribution on a surface located below the observations. This fictitious distribution, named equivalent layer, yields a field that satisfies Laplace's equation and reproduces the observed potential-field data.

The equivalent layer is a consequence of solving the Laplace's equation in the source-free region above the observation surface using the observed field as the Dirichlet boundary condition. Despite the first ideas about the equivalent layer have been known since Poisson's and Green's time, the technique was not used by the geophysicists until the 1960s. In the 1960s, several authors in geophysical literature used the terms equivalent layer and equivalent sources. Roy (1962) uses the term Green's theorem of equivalent layer to draw attention that the observed potential field data can be exactly reproduced by an infinite number of surface physical-property distribution. Dampney (1969) introduced the term equivalent source to define a fictitious stratum located below the observation surface and with finite horizontal dimensions which is formed by a finite discrete set of equivalent sources. In the timeline for magnetic methods of exploration presented by Nabighian et al. (2005b), the "event" of the equivalent-source technique was assigned to Dampney (1969)

even though, as in Dampney's own words, the idea of an equivalent layer has been exploited by other authors such as Daneš (1962), Zidarov (1965) and Bott (1967).

In the beginning, the equivalent layer technique was predominantly used in processing potential-field data. Emilia (1973) showed a wide use of equivalent layer technique in magnetic data processing such as the first and second vertical derivatives, the upward and downward continuations and the reduction to the pole. To our knowledge, Emilia (1973) is the pioneer on the use of the equivalent layer technique in the wavenumber domain by computing the band-pass filtered data and the amplitude spectrum of the data. Emilia (1973) also pointed out that the equivalent layer technique could be used to compute the horizontal and vertical field components, higher-order vertical derivatives, horizontal derivatives, and power and phase spectra.

After Emilia (1973), the equivalent layer technique was used to perform other transformations and to deal with potential-field data measured not only along a profile, but also on a surface. Bott and Ingles (1972) used Poisson's relation and the equivalent layer technique to compute the pseudogravimetric and pseudomagnetic transformations and to estimate the direction of magnetization and the ratio of magnetization to density. Silva (1986) used the equivalent layer technique to perform a reduction to the pole of magnetic data at low magnetic latitudes. By using the equivalent layer technique, Cordell (1992) and Mendonça and Silva (1994) proposed two schemes to interpolate the potential-field data. Recently, Barnes and Lumley (2011) and Barnes (2012, 2014) used the equivalent layer technique to process airborne full-tensor gravity gradient data.

Silva and Hohmann (1984) were one of the first ones that analysed the particular conditions in which the equivalent layer distribution has close association with true geological

sources. They applied the equivalent layer technique to invert reduced-to-the-pole anomalies in order to estimate the geometry and susceptibility variations of purely induced magnetic sources having flat and horizontal top, vertical sides and bottom at infinity.

Since the late 1970s, the equivalent layer technique has been widely used in processing satellite data. To our knowledge, Mayhew (1982) was the pioneer on the use of equivalent layer in satellite-data processing. Instead of processing satellite data by spherical harmonics or Fourier transform methods, Von Frese et al. (1981) used the equivalent layer technique to estimate a spherical distribution of equivalent point sources for processing of both gravity and magnetic anomalies in spherical coordinates system and applied it to obtain geoidal anomalies, vector anomaly components, spatial derivatives, continuations and magnetic pole reductions.

In the wavenumber domain, Emilia (1973) estimated an equivalent source distribution of line of dipoles and, by using the analytical expression of the line of dipoles, the band-pass filtered data and the amplitude spectrum of the data were analytically computed. To calculate a potential field data on a horizontal plane in the wavenumber domain, Pilkington and Urquhart (1990)'s method consists of two steps. In the first one, an equivalent source distribution that fits the data is estimated on a mirror image of the observation surface. In the second step, this irregular mirror image surface is replaced by a horizontal plane and the potential-field data yielded by the equivalent source is computed on the horizontal plane. Pawlowski (1994) proposed a filtering scheme for regional-residual separation method for potential-field data which computes the power spectrum of the data by using two equivalent-source layers to model the residual and regional fields. One equivalent layer models the residual data presumably produced by shallower geological sources and another one models the regional data presumably produced by deeper sources. However, the first complete

work of equivalent layer method in wavenumber was presented by Xia et al. (1993) who also proposed a fast interactive scheme of updating the equivalent source distribution.

By using the analytical relationship between the potential-field data and equivalent physical-property distribution on an hypothetical observational surface, Bhattacharyya and Chan (1977) proposed an iterative scheme for continuing the potential field data between general surface (e.g., from the flight surface to the draped surface). Hansen and Miyazaki (1984) also used the equivalent layer method to accomplish the continuation of the data between arbitrary surfaces. Pedersen (1991) discussed the relationship between potential fields (pseudogravity and magnetic fields) and some equivalent sources (thin sheets and magnetized half-spaces). In the wavenumber domain, Li et al. (2014) proved, under particular conditions, the existence of an all-positive physical property distribution on a planar equivalent layer which has the same purely-induced magnetization direction as the true sources. These authors showed that the use of a positivity constraint on the estimates of the physical-property distribution is sufficient to overcome the low-latitude instability (undesirable artifact of striations) of the reduction-to-the-pole operator defined by an equivalent layer. MacLennan and Li (2013) developed a method for denoising electric field data from frequency-domain controlled-source electromagnetic (CSEM) surveys using an equivalent layer method.

In comparison with the processing potential-field data using the fast Fourier transform (Gunn, 1975), the equivalent layer technique has several advantages. For example, the data do not need to be 1) extrapolated beyond the range of observations (Cordell and Grauch, 1982), 2) equally spaced, or 3) measured on a plane at constant height. However, one serious disadvantage to the application of the equivalent layer technique is the computational cost. For processing large-potential-field data sets via the equivalent layer technique, the

computation cost demanded for building the linear system and for solving the linear inverse problem becomes increasingly important. Several cost-effective methods have developed for processing. In Leão and Silva (1989), the equivalent layer technique is accomplished through a moving-data window and a moving-equivalent-source window which sweep the whole data set. In this fast data-window scheme, the desired transformed data is only computed at the data window center. Xia and Sprowl (1991) and Xia et al. (1993) developed a fast iterative scheme for updating the physical-property distribution within the equivalent layer in the wavenumber and space domains, respectively. To compress the linear system of equations associated with the equivalent layer technique, Li and Oldenburg (2010) used a wavelet compression and Davis and Li (2011) combined an adaptive mesh and wavelet compression. Following the tendency of dealing with large data sets, some methods reduced the number of equivalent sources. Barnes and Lumley (2011) do not compute the full sensitivity matrix of the linear system; rather, for each original  $i$ th row, a set of equivalent sources that lie distant from the  $i$ th observation will be grouped together forming an average equivalent source. Oliveira Jr. et al. (2013) assumed that the physical-property distribution within the equivalent layer can be approximated by a piecewise-polynomial function defined on a set of equivalent-source windows. This procedure leads to a drastic reduction of the linear system of equations that needs to be solved for estimating the physical-property distribution within an equivalent layer.

This article reviews the theoretical bases of the equivalent layer technique and its use in processing potential field data. We start describing the underlying assumptions for the use of this technique in processing gravity and magnetic data. Next, we discuss the mathematical foundations of the equivalent layer and use the Green's identities to prove the well-known upward continuation integral. Then, we present a generalized upward continuation integral

where the layer is an undulating surface. In terms of practical applications of the equivalent layer technique, we address the following issues: 1) the estimation of the physical-property distribution within a discrete equivalent layer; 2) the definition of the harmonic functions describing the potential-field produced by the equivalent sources; and 3) the computational aspects. We also review the theoretical aspects concerning the relationship between the harmonic functions and the physical-property distribution within the equivalent layer.

We deduce, in the space domain, a relationship between the magnetic-moment distribution within an planar equivalent layer of dipoles and the gravity disturbance computed on the equivalent layer. This relationship, which resembles the Poisson's relation, generalizes the previous ones deduced by Pedersen (1991) and Li et al. (2014) in three aspects. First, it does not impose an induced magnetization on the equivalent sources within the equivalent layer. Second, it holds true for all cases in which the magnetization of the dipole layer has the same direction as the true magnetization of the sources, whenever it is purely induced or not. Third, it does not require that the observed total-field anomaly data be on a plane. Finally, we present tests with synthetic data to validate the theoretical aspects, as well as evaluate the performance of the equivalent layer technique in processing potential-field data. For simplicity, we limit our examples to potential-field transformations of total-field anomaly data, by considering cases in which the transformation depends and does not depend on the knowledge of the magnetization direction of the true sources.

## POTENTIAL-FIELD DATA

### Gravity data

The resultant of gravitational force and centrifugal force acting on a body at rest on the Earth's surface is called gravity vector and its intensity is commonly called gravity (Hofmann-Wellenhof and Moritz, 2005). In the case of gravimetry on moving platforms (e.g., airplanes, helicopters, marine vessels), there are additional non-gravitational accelerations due to the vehicle motion, like Coriolis acceleration and high-frequency vibrations (Glennie et al., 2000; Nabighian et al., 2005a; Baumann et al., 2012).

Geophysicists are usually interested in the gravitational component of the observed gravity, which is harmonic and reflects predominantly density variations in the crust and upper mantle (Blakely, 1996). One step of the procedure for isolating the gravitational component of gravity consists in removing the non-gravitational effects due to the vehicle motion and also the time variations of the gravity field (e.g., Earth tides, instrumental drift and barometric pressure changes). If these effects are properly removed, the resultant gravity data can be considered as the sum of a “normal” gravity field and a purely gravitational (and small) “disturbing” field, which is produced by variations in the Earth's internal density distribution. The isolation of this small disturbing field is the main goal in applied geophysics (Blakely, 1996).

Traditionally, the Earth is approximated by a rigid ellipsoid of revolution which is called normal Earth. The normal Earth has the minor axis coincident with the mean Earth's rotation axis, has the same total mass and angular velocity of the Earth and has an undefined internal density distribution (Vaníček and Krakiwsky, 1987; Hofmann-Wellenhof and Moritz, 2005). Similarly to gravity, the resultant of the virtual gravitational and centrifugal forces

exerted by the normal Earth on a body at rest on the Earth's surface is called normal gravity vector and its intensity is commonly called normal gravity. Notice that, according to this traditional definition, the centrifugal component of the normal gravity field is equal to the centrifugal component of the Earth's gravity field if they are evaluated at the same point. The difference between the observed gravity (corrected from non-gravitational effects due to the vehicle motion) and the normal gravity, at the same point, is called gravity disturbance and is a very-well established quantity in geodesy (Hofmann-Wellenhof and Moritz, 2005). The gravity disturbance approximates the gravitational field produced by contrasts between the actual internal density distribution of the Earth and the unknown internal density distribution of the normal Earth. In applied geophysics, these density differences are generally called "anomalous masses" (e.g., Hammer, 1945; LaFehr, 1965) or "gravity sources" (e.g., Blakely, 1996). Here, we opted for using the second term.

In a local- or regional-gravity study, the observed gravity disturbance  $\delta g_i^o$ , at the point  $(x_i, y_i, z_i)$ ,  $i = 1, \dots, N$ , can be considered as the  $z$ -component (or vertical component) of the gravitational attraction exerted by gravity sources. In this case, the observed gravity disturbance (in mGal) produced by a geological body with constant density contrast  $\rho$  can be represented by the following harmonic function

$$\delta g_i^o = k_g G \rho \partial_z \phi_i, \quad (1)$$

where  $G$  is the Newtonian constant of gravitation in  $m^3/(kg s^2)$ ,  $k_g = 10^5$  is a constant factor transforming the gravity disturbance from  $m/s^2$  to milligal (mGal), and  $\partial_z \phi_i$  is a harmonic function representing the first derivative, evaluated at the observation point  $(x_i, y_i, z_i)$ ,  $i = 1, \dots, N$ , of the function

$$\phi(x, y, z) = \int \int \int_v \frac{1}{\sqrt{(x - x')^2 + (y - y')^2 + (z - z')^2}} dv \quad (2)$$

with respect to the variable  $z$ . In this case, the integral is conducted over the coordinates  $x'$ ,  $y'$  and  $z'$  within the volume  $v$  of the gravity source. From now on, we use a Cartesian coordinate system with the  $x$  axis pointing to North, the  $y$  axis pointing to East and the  $z$  axis pointing downward.

## Magnetic data

In magnetic exploration methods, the geomagnetic field is commonly split into the “main field”, “crustal field” and “external field”. The “external field” is predominantly produced by electrical currents located in the ionosphere and magnetosphere and is considered “noise”. The “main field” is the strongest component and, according to the most widely accepted theory, is produced by a self-sustaining dynamo process that takes place within the outer core. Finally, the “crustal field” is produced by the magnetized bodies located in the uppermost (and coldest) layers of the Earth (Langel and Hinze, 1998; Hulot et al., 2015). Generally, the “crustal field” needs to be separated from the remaining components of the geomagnetic field to be interpreted later in applied geophysics. The magnetized bodies located in the subsurface are usually called magnetic sources (Blakely, 1996; Nabighian et al., 2005b).

In magnetic surveys, the commonly measured quantity is the resultant of the main, crustal and external fields. By properly removing the external field and also the magnetic field produced by the moving platforms (e.g., aircraft, ships or helicopters) and cultural noise (e.g., pipelines, railroads, bridges and commercial buildings), the remaining field can be considered as a sum of the main field and the crustal field, which is called “internal field” (Hulot et al., 2015) or “total field” (Blakely, 1996). Here, we opted for using the

second term. The difference between the magnitude of the total field and the magnitude of a suitable model describing the main field (e.g., the IGRF), at the same point, is called “total-field anomaly” (Blakely, 1996; Nabighian et al., 2005b).

Notice that, according to the formal definition of the total-field anomaly, it is not a harmonic function. However, in practical applications, the total-field anomaly can be approximated by a harmonic function. This approximation is valid in local- or regional-scale magnetic studies conducted in a short period of time because, in this case, the main field can be considered as a vector  $\mathbf{F}_0$  with constant direction throughout the study area. In this case,  $\mathbf{F}_0$  can be written as

$$\mathbf{F}_0 = \|\mathbf{F}_0\| \hat{\mathbf{F}}, \quad (3)$$

where  $\|\cdot\|$  denotes the Euclidean norm and

$$\hat{\mathbf{F}} = \begin{bmatrix} \cos(I_0) \cos(D_0) \\ \cos(I_0) \sin(D_0) \\ \sin(I_0) \end{bmatrix} \quad (4)$$

is a unit vector with the constant inclination  $I_0$  and declination  $D_0$  of the local-geomagnetic field. The Euclidean norm of  $\mathbf{F}_0$  is generally many times greater than the Euclidean norm of the crustal field at all observation points on the study area (Blakely, 1996). From these assumptions, the observed total-field anomaly  $\Delta T_i^o$  at any point  $(x_i, y_i, z_i)$ ,  $i = 1, \dots, N$ , can be described by the following harmonic function:

$$\Delta T_i^o = \hat{\mathbf{F}}^\top \mathbf{B}_i, \quad (5)$$

where  $\mathbf{B}_i$  represents the magnetic induction produced by the magnetic sources at the point  $(x_i, y_i, z_i)$ ,  $i = 1, \dots, N$  and the  $^\top$  stands for transpose.

Let’s consider a uniformly magnetized source with volume  $v$  and constant magnetization

vector  $\mathbf{m}$ . Here, the magnetization intensity is given in ampere per meter (A/m) and the coordinates in meter (m). The magnetic induction  $\mathbf{B}_i$  (in nT) produced by this source at the point  $(x_i, y_i, z_i)$ ,  $i = 1, \dots, N$ , can be represented as follows:

$$\mathbf{B}_i = k_m \frac{\mu_0}{4\pi} \mathbf{M}_i \mathbf{m}, \quad (6)$$

where  $\mu_0 = 4\pi \cdot 10^{-7}$  H/m is the magnetic constant,  $k_m = 10^9$  is a constant factor transforming the magnetic induction from tesla (T) to nanotesla (nT), and  $\mathbf{M}_i$  is a matrix given by

$$\mathbf{M}_i = \begin{bmatrix} \partial_{xx}\phi_i & \partial_{xy}\phi_i & \partial_{xz}\phi_i \\ \partial_{xy}\phi_i & \partial_{yy}\phi_i & \partial_{yz}\phi_i \\ \partial_{xz}\phi_i & \partial_{yz}\phi_i & \partial_{zz}\phi_i \end{bmatrix}, \quad (7)$$

with  $\partial_{\alpha\beta}\phi_i$ ,  $\alpha = x, y, z$ ,  $\beta = x, y, z$ , being the second derivatives, evaluated at the coordinates  $(x_i, y_i, z_i)$ ,  $i = 1, \dots, N$ , of the function  $\phi(x, y, z)$  (equation 2) with respect to the variables  $x, y$  and  $z$ . In this case, this integral in equation 2 is evaluated over the coordinates  $x', y'$  and  $z'$  within the volume  $v$  of the magnetic source. Finally, by using the magnetic induction  $\mathbf{B}_i$  (equation 6) with the magnetization vector  $\mathbf{m} = m \hat{\mathbf{m}}$ , the observed total-field anomaly  $\Delta T_i^o$  (equation 5) can be rewritten as follows:

$$\Delta T_i^o = k_m \frac{\mu_0}{4\pi} m \hat{\mathbf{F}}^\top \mathbf{M}_i \hat{\mathbf{m}}, \quad (8)$$

where  $m$  the magnetization intensity and  $\hat{\mathbf{m}}$  is a unit vector.

Equation 8 describes the total-field anomaly produced by an uniformly magnetized source. Notice that both the magnetization of the source and the local-geomagnetic field have an arbitrary direction. In this general case, the total-field anomaly oscillates from negative to positive values, so that its maxima are not placed above the magnetic source. Because of this oscillating pattern, the total-field anomaly cannot be directly used by the

interpreter to locate the source. To overcome this problem, Baranov (1957) proposed a method called reduction to the pole. This method transforms a total-field anomaly  $\Delta T_i^o$  (equation 8) into a simpler one given by

$$\Delta T_i^P = k_m \frac{\mu_0}{4\pi} m \partial_{zz} \phi_i, \quad (9)$$

which represents the total-field anomaly that would be produced by the magnetic source if it were magnetized in the same direction as the local-geomagnetic field at the pole. In this situation, both the local-geomagnetic field and the magnetization of the source would be vertical and, consequently, the vectors  $\hat{\mathbf{F}}$  and  $\hat{\mathbf{m}}$  (equation 8) would be equal to  $\mathbf{u} = [0 \ 0 \ 1]^\top$ . Note that  $\Delta T_i^P$  (equation 9) depends on the exact position and volume of the source, which we never know in practice. Along the manuscript, we refer to  $\Delta T_i^P$  as “RTP anomaly”.

As pointed out by Baranov (1957), this equation represents the particular case of Poisson’s relation in which the magnetization of the source is vertical. In this case,  $\Delta T_i^P$  (equation 9) is a predominantly positive anomaly which is proportional to the vertical gradient of the gravitational attraction that would be produced by the magnetic source if it had a positive and constant density contrast equal to  $\rho = 1/(k_g G)$ , where  $G$  is the gravitational constant and  $k_g$  is a positive constant (equation 1).

## MATHEMATICAL FOUNDATIONS

### Green’s third identity

Let  $v$  be a regular region of space with boundary defined by a closed regular surface  $S$  (Figure 1). Let’s also consider a scalar function  $U(x, y, z)$  satisfying three conditions: 1) it is continuous at all points of  $v$ , including its boundary  $S$ , 2) its second derivatives exist

and are continuous at all point of  $v$  (not necessarily on  $S$ ) and 3) it is regular at infinity. We refer the reader to Kellogg (1929) for a proper definition of regular regions, regular surfaces and functions that are regular at infinity. In this case, according to the Green's third identity (Kellogg, 1929),

$$U(x_i, y_i, z_i) = -\frac{1}{4\pi} \iiint_v \frac{1}{r} \nabla^2 U(x, y, z) dv - \frac{1}{4\pi} \iint_S U(x, y, z) \partial_n \frac{1}{r} - \frac{1}{r} \partial_n U(x, y, z) dS \quad (10)$$

where the variables  $x_i, y_i$  and  $z_i$  are the Cartesian coordinates of an arbitrarily fixed point within  $v$  (Figure 1). In equation 10, the integrals are conducted over the variables  $x, y$  and  $z$ , which represent either a volume element of  $v$  or a surface element of  $S$ . The terms on the right side of equation 10 are

$$\frac{1}{r} \equiv \frac{1}{\sqrt{(x - x_i)^2 + (y - y_i)^2 + (z - z_i)^2}}, \quad (11)$$

which is the inverse distance from the fixed point  $(x_i, y_i, z_i)$  (black dot in Figure 1) to the integration point  $(x, y, z)$ , the Laplacian of the function  $U(x, y, z)$ , which is given by

$$\nabla^2 U(x, y, z) = \partial_{xx}^2 U(x, y, z) + \partial_{yy}^2 U(x, y, z) + \partial_{zz}^2 U(x, y, z), \quad (12)$$

where  $\partial_{\alpha\beta}^2 U(x, y, z) \equiv \frac{\partial^2 U(x, y, z)}{\partial\alpha\partial\beta}$ ,  $\alpha = x, y, z$ ,  $\beta = x, y, z$ , and the normal derivatives

$$\partial_n \frac{1}{r} \equiv \nabla \frac{1}{r} \cdot \hat{\mathbf{n}} \quad (13)$$

and

$$\partial_n U(x, y, z) \equiv \nabla U(x, y, z) \cdot \hat{\mathbf{n}}. \quad (14)$$

In equations 13 and 14, the symbol  $(\cdot)$  denotes the dot product of vectors,  $\hat{\mathbf{n}}$  is the outward-pointing normal to the surface  $S$  at a point  $(x, y, z)$  and, finally,  $\nabla \frac{1}{r}$  and  $\nabla U(x, y, z)$  represent, respectively, the gradient of the functions  $\frac{1}{r}$  (equation 11) and  $U(x, y, z)$ , both with respect to the variables  $x, y$  and  $z$ .

## Classical upward continuation integral

Let's  $U(x, y, z)$  be a harmonic function at all points  $(x, y, z)$  within  $v$  (Figure 1). In this case, the first term in equation 10 drops and the Green's third identity can be rewritten as

$$U(x_i, y_i, z_i) = -\frac{1}{4\pi} \iint_S U(x, y, z) \partial_n \frac{1}{r} - \frac{1}{r} \partial_n U(x, y, z) dS . \quad (15)$$

Notice that, in equation 15, the variables  $x$ ,  $y$  and  $z$  represent the Cartesian coordinates of an arbitrary point belonging to the surface  $S$  (Figure 1).

Let's split the surface  $S$  into two surfaces  $S_1$  and  $S_2$ , where  $S_1$  is a hemisphere with radius  $R$  and  $S_2$  is a horizontal plane with constant vertical coordinate  $z = z_c$  (Figure 2). We stress that these two surfaces do not have any relationship with the equipotential surfaces of the harmonic function  $U(x, y, z)$ . In this case, the surface integral can also be split as follows

$$U(x_i, y_i, z_i) = I_1 + I_2 , \quad (16)$$

where

$$I_1 = -\frac{1}{4\pi} \iint_{S_1} U(x, y, z) \partial_n \frac{1}{r} - \frac{1}{r} \partial_n U(x, y, z) dS_1 \quad (17)$$

and

$$I_2 = -\frac{1}{4\pi} \iint_{S_2} U(x, y, z_c) \partial_z \frac{1}{r} - \frac{1}{r} \partial_z U(x, y, z_c) dS_2 . \quad (18)$$

Notice that, in equation 17, the outward normal  $\hat{\mathbf{n}} = \hat{\mathbf{n}}_1$  (Figure 2) has a constant radial direction whereas, in equation 18, the outward normal  $\hat{\mathbf{n}} = \hat{\mathbf{n}}_2$  (Figure 2) has the same direction as the vertical axis  $z$ , so that  $\partial_n = \partial_z$ . By making  $R \rightarrow \infty$ , the integral on the surface  $S_1$  (equation 17) vanishes and, consequently, equation 16 reduces to

$$U(x_i, y_i, z_i) = -\frac{1}{4\pi} \int_{-\infty}^{+\infty} \int_{-\infty}^{+\infty} U(x, y, z_c) \partial_z \frac{1}{r} - \frac{1}{r} \partial_z U(x, y, z_c) dx dy , \quad (19)$$

where  $z_i = z_c - \Delta z$ , with  $\Delta z > 0$  (Figure 2). Equation 19 shows that, given the values of a harmonic function and its vertical derivative on a horizontal plane at  $z = z_c$ , it is possible to calculate the value of this harmonic function at any point located above this horizontal plane. For practical purposes, it is convenient to manipulate equation 19 in order to remove the vertical derivative  $\partial_z U(x, y, z_c)$ . To do this, let's first define the function

$$\frac{1}{\ell} \equiv \frac{1}{\sqrt{(x - x_i)^2 + (y - y_i)^2 + (z - z_s)^2}} \quad (20)$$

representing the inverse distance between the point  $(x_i, y_i, z_s)$  and an arbitrary point on the plane  $S_2$  (Figure 2). Notice that the point  $(x_i, y_i, z_s)$  (open circle in Figure 2) can be considered a mirror of the point  $(x_i, y_i, z_i)$  (black dot in Figure 2) with respect to the horizontal plane  $S_2$  because  $z_s = z_c + \Delta z$  and  $z_i = z_c - \Delta z$ . Besides,  $\frac{1}{\ell}$  (equation 20) is harmonic at all points  $(x, y, z)$  in  $v$ . Then, by applying the Green's second identity (Kellogg, 1929), we obtain

$$\iiint_v U(x, y, z) \nabla^2 \frac{1}{\ell} - \frac{1}{\ell} \nabla^2 U(x, y, z) dv = \iint_S U(x, y, z) \partial_n \frac{1}{\ell} - \frac{1}{\ell} \partial_n U(x, y, z) dS. \quad (21)$$

By multiplying both sides in equation 21 by  $1/4\pi$  and recalling that  $U(x, y, z)$  and  $\frac{1}{\ell}$  are harmonic at all points within  $v$ , we have

$$0 = \frac{1}{4\pi} \iint_S U(x, y, z) \partial_n \frac{1}{\ell} - \frac{1}{\ell} \partial_n U(x, y, z) dS \quad (22)$$

and, subsequently, by adding equation 22 to equation 15 we get

$$U(x_i, y_i, z_i) = -\frac{1}{4\pi} \iint_S U(x, y, z) \left( \partial_n \frac{1}{r} - \partial_n \frac{1}{\ell} \right) - \left( \frac{1}{r} - \frac{1}{\ell} \right) \partial_n U(x, y, z) dS. \quad (23)$$

Now, similarly to what was previously done, let's split the surface  $S$  into two surfaces  $S_1$  and  $S_2$ , according to the Figure 2, and let's also tend  $R$  to infinite. Consequently, the integral over the surface  $S_1$  vanishes and equation 23 becomes

$$U(x_i, y_i, z_i) = -\frac{1}{4\pi} \int_{-\infty}^{+\infty} \int_{-\infty}^{+\infty} U(x, y, z_c) \left( \partial_z \frac{1}{r} - \partial_z \frac{1}{\ell} \right) - \left( \frac{1}{r} - \frac{1}{\ell} \right) \partial_z U(x, y, z_c) dx dy. \quad (24)$$

The two terms between parenthesis in the surface integral shown in equation 24 deserve special attention because they assume specific values on this plane. Notice that the derivative of the functions  $\frac{1}{r}$  (equation 11) and  $\frac{1}{\ell}$  (equation 20) with respect to the variable  $z$  are:

$$\partial_z \frac{1}{r} \equiv \frac{-(z - z_i)}{[(x - x_i)^2 + (y - y_i)^2 + (z - z_i)^2]^{\frac{3}{2}}} \quad (25)$$

and

$$\partial_z \frac{1}{\ell} \equiv \frac{-(z - z_s)}{[(x - x_i)^2 + (y - y_i)^2 + (z - z_s)^2]^{\frac{3}{2}}}. \quad (26)$$

Then, by evaluating equations 11, 20, 25 and 26 at a point  $(x, y, z)$ , with  $z = z_c$ , and recalling that  $z_i = z_c - \Delta z$  and  $z_s = z_c + \Delta z$  (Figure 2), we can easily verify that  $\frac{1}{r} = \frac{1}{\ell}$  and  $\partial_z(1/r) = -\partial_z(1/\ell)$ . Consequently, equation 24 can be rewritten as

$$U(x_i, y_i, z_i) = \frac{z_c - z_i}{2\pi} \int_{-\infty}^{+\infty} \int_{-\infty}^{+\infty} \frac{U(x, y, z_c)}{[(x_i - x)^2 + (y_i - y)^2 + (z_i - z_c)^2]^{\frac{3}{2}}} dx dy, \quad z_c > z_i. \quad (27)$$

In the geophysical literature, several authors have presented different versions of equation 27 (Skeels, 1947; Henderson and Zietz, 1949; Henderson, 1960; Roy, 1962; Bhattacharyya, 1967; Henderson, 1970; Twomey, 1977; Blakely, 1996). Here, by following Henderson (1960, 1970), we call equation 27 as the upward continuation integral.

According to the classical upward continuation integral (equation 27), the values of the harmonic function  $U(x_i, y_i, z_i)$  at any point  $(x_i, y_i, z_i)$ ,  $z_i < z_c$ , can be exactly reproduced by the convolution between its values  $U(x, y, z_c)$  and the vertical derivative of the function  $1/r$  (equation 11), both evaluated on the horizontal plane  $z = z_c$  (Figure 2). From the physical point of view, the harmonic function  $U(x_i, y_i, z_i)$  represents the scalar potential produced by a planar and continuous dipole layer having vertical magnetization and a unique magnetic moment distribution equal to  $-U(x, y, z_c)/2\pi$ .

Notice that, according to the classical upward continuation integral (equation 27), any

spatial derivative of the harmonic function  $U(x_i, y_i, z_i)$  can be obtained by properly differentiating the integrand. Then, by assuming the knowledge of  $U(x, y, z_c)$  on the horizontal plane  $z = z_c$  (Figure 2), it is possible to compute not only  $U(x_i, y_i, z_i)$ , but also any of its spatial derivatives at any point  $(x_i, y_i, z_i)$ ,  $z_i < z_c$ .

## GENERALIZED UPWARD CONTINUATION INTEGRAL

### Mathematical development

This section attempts to generalize the classical upward continuation integral (equation 27) to the case in which the harmonic function  $U(x_i, y_i, z_i)$  is represented by an integral conducted over an undulating surface. To do this, let's first define a regular surface (see Kellogg, 1929) on which any point has Cartesian coordinates  $(x', y', z')$  and

$$z' = f(x', y'), \quad z_i < z' \leq z_c, \quad (28)$$

where  $f(x', y')$  is a function with continuous and bounded partial derivatives of first and second orders. Let's also consider that the harmonic function  $U(x, y, z_c)$ , evaluated on the horizontal plane  $z = z_c$  (Figure 2), can be represented by a surface integral

$$U(x, y, z_c) = \int_{-\infty}^{+\infty} \int_{-\infty}^{+\infty} \tilde{p}(x', y', z') g(x - x', y - y', z_c - z') dS', \quad (29)$$

where  $z'$  is defined by equation 28, the surface element  $dS'$  is given by (Kellogg, 1929; Bhattacharyya and Chan, 1977; Jeffreys and Jeffreys, 2000)

$$dS' = [1 + (\partial_{x'} f)^2 + (\partial_{y'} f)^2]^{\frac{1}{2}} dx' dy', \quad (30)$$

$g(x - x', y - y', z_c - z')$  is a harmonic function that tends to zero as the distance between the points  $(x, y, z_c)$  and  $(x', y', z')$  tends to infinite and  $\tilde{p}(x', y', z')$  is a generic bounded function

that satisfies the necessary conditions for the existence of the surface integral. In equation 30,  $\partial_{\alpha'} f \equiv \frac{\partial f}{\partial \alpha'}(x', y')$ ,  $\alpha' = x', y'$ . By substituting the surface element  $dS'$  (equation 30) into equation 29, we obtain

$$U(x, y, z_c) = \int_{-\infty}^{+\infty} \int_{-\infty}^{+\infty} p(x', y', z') g(x - x', y - y', z_c - z') dx' dy', \quad (31)$$

where

$$p(x', y', z') = [1 + (\partial_{x'} f)^2 + (\partial_{y'} f)^2]^{\frac{1}{2}} \tilde{p}(x', y', z'). \quad (32)$$

By substituting equation 31 into the classical upward continuation integral (equation 27) and conveniently changing the integration order, we obtain

$$U(x_i, y_i, z_i) = \int_{-\infty}^{+\infty} \int_{-\infty}^{+\infty} p(x', y', z') \left\{ \frac{1}{2\pi} \int_{-\infty}^{+\infty} \int_{-\infty}^{+\infty} \frac{(z_c - z_i) g(x - x', y - y', z_c - z')}{[(x_i - x)^2 + (y_i - y)^2 + (z_i - z_c)^2]^{\frac{3}{2}}} dx dy \right\} dx' dy'. \quad (33)$$

For convenience, we define new variables  $\epsilon = x - x'$ ,  $\eta = y - y'$  and  $\zeta = z_c - z'$  and substitute them into the term in brackets in equation 33. By noting that  $\zeta > (z_i - z')$  and comparing the result with the classical upward continuation integral (equation 27), we conclude that

$$g(x_i - x', y_i - y', z_i - z') = \frac{1}{2\pi} \int_{-\infty}^{+\infty} \int_{-\infty}^{+\infty} \frac{[\zeta - (z_i - z')] g(\epsilon, \eta, \zeta)}{\{[(x_i - x') - \epsilon]^2 + [(y_i - y') - \eta]^2 + [(z_i - z') - \zeta]^2\}^{\frac{3}{2}}} d\epsilon d\eta. \quad (34)$$

By substituting the term in brackets in equation 33 by equation 34, we obtain a generalized upward continuation integral given by

$$U(x_i, y_i, z_i) = \int_{-\infty}^{+\infty} \int_{-\infty}^{+\infty} p(x', y', z') g(x_i - x', y_i - y', z_i - z') dx' dy'. \quad (35)$$

This approach is based on Mendonça (1992), who deduced a discrete version of the generalized upward continuation integral (equation 35).

## Relationship between the harmonic function and the physical property distribution

In equation 35, the function  $p(x', y', z')$  represents the physical property distribution on the continuous and undulating surface  $z' = f(x', y')$ . The observed potential field  $U(x_i, y_i, z_i)$  and the choice of the harmonic function  $g(x_i - x', y_i - y', z_i - z')$  determine the physical meaning of the generalized upward continuation integral. This choice, in turn, can be conveniently made according to the specificities of the problem to be solved. Generally, the harmonic function  $g(x_i - x', y_i - y', z_i - z')$  (equation 35) is written in terms of the inverse distance function

$$\theta(x - x', y - y', z - z') = \frac{1}{r'}, \quad (36)$$

its first derivatives

$$\partial_\alpha \theta(x - x', y - y', z - z') = \frac{\alpha' - \alpha}{(r')^3}, \quad (37)$$

second derivatives

$$\partial_{\alpha\beta} \theta(x - x', y - y', z - z') = \begin{cases} \frac{3(\alpha - \alpha')^2}{(r')^5} - \frac{1}{(r')^3}, & \alpha = \beta \\ \frac{3(\alpha - \alpha')(\beta - \beta')}{(r')^5}, & \alpha \neq \beta \end{cases}, \quad (38)$$

and third derivatives

$$\partial_{\alpha\beta\gamma} \theta(x - x', y - y', z - z') = \begin{cases} \frac{9(\alpha - \alpha')}{(r')^5} - \frac{15(\alpha - \alpha')^3}{(r')^7}, & \alpha = \beta = \gamma \\ \frac{3(\gamma - \gamma')}{(r')^5} - \frac{15(\alpha - \alpha')^2(\gamma_i - \gamma')}{(r')^7}, & \alpha = \beta \neq \gamma \\ \frac{15(\alpha - \alpha')(\beta - \beta')(\gamma - \gamma')}{(r')^7}, & \alpha \neq \beta, \alpha \neq \gamma, \beta \neq \gamma \end{cases}, \quad (39)$$

where  $\alpha = x, y, z$ ,  $\beta = x, y, z$ ,  $\gamma = x, y, z$ ,  $\alpha' = x', y', z'$ ,  $\beta' = x', y', z'$  and  $\gamma' = x', y', z'$ . In equations 36–39,

$$r' = [(x - x')^2 + (y - y')^2 + (z - z')^2]^{\frac{1}{2}} \quad (40)$$

represents the Euclidean distance between a point  $(x, y, z)$  and an observation point  $(x', y', z')$  on the undulating surface  $z'$  (equation 28). In the two subsections that follow we present examples of the relationship between the harmonic function and the physical property distribution, as well as some theoretical implications.

### Relationship between the generalized and the classical upward continuation integrals

Consider the particular case in which the harmonic function  $g(x_i - x', y_i - y', z_i - z')$  in equation 35 is given by equation 37, with  $\alpha = z$ . Additionally, suppose that  $z'$  (equation 28) tends to the constant  $z_c$  (Figura 2) at all points  $(x', y')$ . In this case, the horizontal derivatives  $\partial_{x'} f$  and  $\partial_{y'} f$  (equations 30 and 32) tend to zero and the generalized upward continuation integral (equation 35) is given by

$$U(x_i, y_i, z_i) = \int_{-\infty}^{+\infty} \int_{-\infty}^{+\infty} p(x', y', z_c) \partial_z \theta(x_i - x', y_i - y', z_i - z_c) dx' dy', \quad (41)$$

where  $p(x', y', z_c) = \tilde{p}(x', y', z_c)$  (equation 32). Finally, by comparing equation 41 with the classical upward continuation integral (equation 27), it is apparent that the physical property distribution  $p(x', y', z_c)$  (equation 32) assumes the particular form given by

$$p(x', y', z_c) = \frac{U(x', y', z_c)}{2\pi}. \quad (42)$$

### Theoretical magnetic moment distribution in a continuous double layer

In this section, we will analyse the particular case in which the generalized upward continuation integral (equation 35) is used to describe the observed total-field anomaly  $\Delta T_i^o$  (equation 8) by a continuous double layer having a magnetic moment distribution with constant direction and variable intensity. Let's also consider that the equivalent is defined by

a horizontal plane located at a constant depth  $z' = z_c$ . In this case, the harmonic function  $g(x_i - x', y_i - y', z_i - z')$  is given by

$$g(x_i - x', y_i - y', z_i - z_c) = k_m \frac{\mu_0}{4\pi} \hat{\mathbf{F}}^\top \mathbf{H}_i \hat{\mathbf{h}}, \quad (43)$$

where  $\hat{\mathbf{F}}$  is the unit vector (equation 4) having the same direction as the local-geomagnetic field  $\mathbf{F}_0$  (equation 3),  $\hat{\mathbf{h}}$  is a constant unit vector given by

$$\hat{\mathbf{h}} = \begin{bmatrix} \cos(I) \cos(D) \\ \cos(I) \sin(D) \\ \sin(I) \end{bmatrix}, \quad (44)$$

which represents the arbitrary magnetization direction with constant inclination  $I$  and constant declination  $D$  within the continuous double layer and the matrix  $\mathbf{H}_i$  is given by

$$\mathbf{H}_i = \begin{bmatrix} \partial_{xx}\theta_i & \partial_{xy}\theta_i & \partial_{xz}\theta_i \\ \partial_{xy}\theta_i & \partial_{yy}\theta_i & \partial_{yz}\theta_i \\ \partial_{xz}\theta_i & \partial_{yz}\theta_i & \partial_{zz}\theta_i \end{bmatrix}, \quad (45)$$

where the partial derivatives of second order  $\partial_{\alpha\beta}\theta_i \equiv \partial_{\alpha\beta}\theta(x_i - x', y_i - y', z_i - z_c)$ ,  $\alpha = x, y, z$ ,  $\beta = x, y, z$ , are defined according to equation 38. Mathematically, the harmonic function  $g(x_i - x', y_i - y', z_i - z_c)$  (equation 43) represents the product of  $(k_m \mu_0/4\pi)$  and the second directional derivative of the function  $\theta(x_i - x', y_i - y', z_i - z_c)$  (equation 36) taken along the directions defined by the unit vectors  $\hat{\mathbf{F}}$  and  $\hat{\mathbf{h}}$ . From the physical point of view, this harmonic function represents the total-field anomaly produced, at the observation point  $(x_i, y_i, z_i)$ ,  $i = 1, \dots, N$ , by a dipole that has unit magnetic moment and is located at a point  $(x', y', z_c)$ , where  $z_c > z_i$ . By using such harmonic functions, the function  $p(x', y', z_c)$  (equation 32) can be considered the magnetic moment intensity (in  $\text{Am}^2$ ) per unit area within the continuous double layer. For convenience, the unit vector  $\hat{\mathbf{h}}$  (equations 43 and

44) can also be written as

$$\hat{\mathbf{h}} = \mathbf{R}\hat{\mathbf{m}}, \quad (46)$$

where  $\hat{\mathbf{m}}$  (equation 8) is a unit vector with the same direction as the true magnetization of the source and  $\mathbf{R}$  is a  $3 \times 3$  matrix obtained from Euler's rotation theorem. This theorem states that any rotation can be parametrized by using three parameters called Euler angles (Goldstein et al., 1980).

Notice that, if the double layer have the same magnetization direction as the true magnetic source, the rotation matrix  $\mathbf{R}$  (equation 46) is equal to the identity matrix.

By combining equations 35, 43 and 46, the observed total-field anomaly  $\Delta T_i^o$  (equation 8) can be rewritten as

$$\Delta T_i^o = \int_{-\infty}^{+\infty} \int_{-\infty}^{+\infty} p(x', y', z_c) \left[ k_m \frac{\mu_0}{4\pi} \hat{\mathbf{F}}^\top \mathbf{H}_i \hat{\mathbf{m}} \right] dx' dy', \quad (47)$$

which represents the total-field anomaly produced by a continuous double layer with the same magnetization direction as the true magnetic source. In this case, according to equation 47, the total-field anomaly  $\Delta T_i^P$  (equation 9) can be rewritten as follows:

$$\Delta T_i^P = \int_{-\infty}^{+\infty} \int_{-\infty}^{+\infty} p(x', y', z_c) \left[ k_m \frac{\mu_0}{4\pi} \partial_{zz} \theta(x_i - x', y_i - y', z_i - z_c) \right] dx' dy', \quad (48)$$

where  $\partial_{zz} \theta(x_i - x', y_i - y', z_i - z_c)$  is defined in equation 38. By comparing equations 9 and 48, we obtain

$$m \partial_{zz} \phi_i = \int_{-\infty}^{+\infty} \int_{-\infty}^{+\infty} p(x', y', z_c) \partial_{zz} \theta(x_i - x', y_i - y', z_i - z_c) dx' dy', \quad (49)$$

where  $\partial_{zz} \phi_i$  is the second derivative, evaluated at the observation point  $(x_i, y_i, z_i)$ ,  $i = 1, \dots, N$ , of the harmonic function  $\phi(x, y, z)$  (equation 2) with respect to the variable  $z$ . In this case, the integral in equation 2 is conducted over the volume of the magnetic source.

Notice that equation 49 can be obtained by differentiating the following equation

$$m \partial_z \phi_i = \int_{-\infty}^{+\infty} \int_{-\infty}^{+\infty} p(x', y', z_c) \partial_z \theta(x_i - x', y_i - y', z_i - z_c) dx' dy' \quad (50)$$

with respect to the variable  $z$ , where  $\partial_z \phi_i$  represents the first derivative of the function  $\phi(x, y, z)$  (equation 2) with respect to the variable  $z$  and evaluated at the observation point  $(x_i, y_i, z_i)$ . Then, according to equations 27 and 41, we conclude that equation 50 represents the upward continuation of the harmonic function  $(m \partial_z \phi_i)$  and, consequently,

$$p(x', y', z_c) = \frac{m}{2\pi} \partial_z \phi(x', y', z_c), \quad (51)$$

where  $\partial_z \phi(x', y', z_c)$  is the first derivative, evaluated on the double layer, of the function  $\phi(x, y, z)$  (equation 2) with respect to the variable  $z$ .

It is also worth noting that the function  $\partial_z \phi(x', y', z_c)$  is positive at all points  $(x', y', z_c)$  on the planar equivalent layer. By using equation 1,  $p(x', y', z_c)$  (equation 51) can be rewritten as follows

$$p(x', y', z_c) = \frac{m}{2\pi k_g \rho G} \delta g(x', y', z_c), \quad (52)$$

where  $\delta g(x', y', z_c)$  is the gravity disturbance that would be produced by the magnetic source, at the point  $(x', y', z_c)$  on the equivalent layer, if it had a constant density contrast  $\rho$ .

We call attention that equation 52 represents the magnetic moment distribution (per unit area) distribution of the continuous double layer which has the same magnetization direction as the true magnetic source and reproduces the observed total-field anomaly  $\Delta T_i^o$  (equation 47). The remarkable aspect in equation 52 is that  $p(x', y', z_c)$  is all positive because the constant  $m/(2\pi k_g G)$  is positive, as well as the ratio  $\delta g(x', y', z_c)/\rho$  is positive at all points  $(x', y', z_c)$  on the horizontal plane defining the continuous double layer. Notice

that equation 52 was deduced by considering that the magnetization intensity  $m$  and density  $\rho$  are constant throughout all the magnetic sources.

This relationship is similar to that one presented by Pedersen (1991) and Li et al. (2014). By following different approaches in the wavenumber domain, they proved the existence of an all-positive magnetic moment distribution within a continuous double layer. Their approach, however, is valid only for the case in which the observed total-field anomaly is produced by magnetic sources having a purely and vertical induced magnetization. They also considered a planar double layer which is parallel to a horizontal plane containing the observed total-field anomaly. Under these assumptions, Pedersen (1991) and Li et al. (2014) concluded that the magnetic moment distribution within the continuous double layer is all-positive and proportional to the pseudogravity anomaly produced by the source on the plane of the double layer. Equation 52 generalizes this positivity condition because it (1) does not impose an induced magnetization on the equivalent sources within the equivalent layer, (2) holds true for all cases in which the magnetization of the dipole layer has the same direction as the true magnetization of the sources, whenever it is purely induced or not, and (3) does not require that the observed total-field anomaly data be on a plane.

By substituting this theoretical magnetic-moment distribution  $p(x', y', z_c)$  (equation 52) into the total-field anomaly (equation 47), we obtain

$$\Delta T_i^o = \frac{1}{2\pi} \frac{k_m m (\mu_0/4\pi)}{k_g \rho G} \int_{-\infty}^{+\infty} \int_{-\infty}^{+\infty} \delta g(x', y', z_c) \hat{\mathbf{F}}^\top \mathbf{H}_i \hat{\mathbf{m}} dx' dy'. \quad (53)$$

Equation 53 is substantially different from the Poisson's relation (Garland, 1951; Baranov, 1957; Cordell and Taylor, 1971; Chandler et al., 1981; Blakely, 1996; Mendonça, 2004), because it relates the total-field anomaly  $\Delta T_i^o$  at an observation point  $(x_i, y_i, z_i)$  and the gravity disturbance  $\delta g(x', y', z_c)$  that would be produced by the magnetic sources, at the

planar surface defining the equivalent layer, if they had a constant density contrast  $\rho$ .

Equation 53 can be generalized to the case in which the magnetization intensity  $m$  and density  $\rho$  vary within the sources. This can be done by first dividing the magnetic sources into  $Q$  small volume elements  $dv^k$ ,  $k = 1, \dots, Q$ , inside which the magnetization intensity  $m^k$  and density  $\rho^k$  are constant. Then, we use equation 53 to represent the total-field anomaly  $\Delta T_i^k$  produced by each volume element  $dv^k$  at the observation point  $(x_i, y_i, z_i)$ .

By summing the total-field anomalies  $\Delta T_i^k$ , we obtain

$$\Delta T_i^o = \frac{1}{2\pi} \frac{k_m (\mu_0/4\pi)}{k_g G} \sum_{k=1}^Q \left[ \int_{-\infty}^{+\infty} \int_{-\infty}^{+\infty} \frac{m^k \delta g^k(x', y', z_c)}{\rho^k} \hat{\mathbf{F}}^\top \mathbf{H}_i \hat{\mathbf{m}} dx' dy' \right], \quad (54)$$

or, alternatively,

$$\Delta T_i^o = \frac{1}{2\pi} \frac{k_m (\mu_0/4\pi)}{k_g G} \int_{-\infty}^{+\infty} \int_{-\infty}^{+\infty} \left[ \sum_{k=1}^Q \frac{m^k \delta g^k(x', y', z_c)}{\rho^k} \right] \hat{\mathbf{F}}^\top \mathbf{H}_i \hat{\mathbf{m}} dx' dy', \quad (55)$$

where  $\delta g^k(x', y', z_c)$  represents the gravity disturbance that would be produced by the  $k$ th volume element  $dv^k$ , at the point  $(x', y', z_c)$  on the equivalent layer, if it had a constant density contrast  $\rho^k$ .

By comparing equation 55 with equation 53, we can see that the theoretical magnetic-moment distribution (equation 52) can be generalized as follows

$$p(x', y', z_c) = \frac{1}{2\pi k_g G} \sum_{k=1}^Q \left[ \frac{m^k \delta g^k(x', y', z_c)}{\rho^k} \right]. \quad (56)$$

Notice that the ratio  $\delta g^k(x', y', z_c)/\rho^k$  is positive at all points on the planar equivalent layer, for any  $k$ , where  $k = 1, \dots, Q$ . Consequently, the generalized magnetic-moment distribution (equation 56) is all-positive as well. Equations 54, 55, and 56 show that the magnetic-moment distribution within a planar equivalent layer of dipoles with the same magnetization direction as the true magnetic sources is all-positive even in the case that the magnetization intensity varies within the magnetic sources.

## EQUIVALENT LAYER TECHNIQUE

### Discrete equivalent layer and practical considerations

In geophysics, the classical (equation 27) or generalized (equation 35) upward continuation integrals are commonly used to calculate, for example, the upward continuation or interpolation of different potential-field data  $U(x_i, y_i, z_i)$ , e.g., gravity disturbance  $\delta g_i^o$  (equation 1) or total-field anomaly  $\Delta T_i^o$  (equation 8). The potential-field data may be measured on an irregular grid of observation points  $(x_i, y_i, z_i)$ ,  $i = 1, \dots, N$ , that may be located on an uneven surface such as the Earth's surface, for a ground survey, or a draped surface, for an airborne survey. We emphasize that the use of these integrals implicitly assumes that the potential-field data are harmonic. Therefore, the data must be previously processed with the purpose of supporting this assumption.

According to the classical (equation 27) or the generalized (equation 35) upward continuation integrals, any observed potential-field data  $d_i^o \equiv U(x_i, y_i, z_i)$  can be exactly reproduced by a theoretical and fictitious continuous layer having a physical property distribution defined by  $p(x', y', z')$  (equation 32). In other words, it is possible to establish a fictitious layer which has a theoretical physical-property distribution and exactly reproduces the observed potential-field data that is produced by the actual and unknown geological sources located in the subsurface. In geophysics, this fictitious layer is commonly called “equivalent layer”. These integrals (equations 27 or 35), however, cannot be used in practical applications because we are not able to determine the physical property distribution  $p(x', y', z')$  in a continuous equivalent layer reproducing a discrete set of potential-field observations  $d_i^o$ ,  $i = 1, \dots, N$ .

In practical applications, the continuous equivalent layer is approximated by a discrete

set of sources (usually punctual sources) located at points  $(x_j, y_j, z_j)$ ,  $j = 1, \dots, M$ . The physical property distribution within the discrete equivalent layer is represented by the parameter vector  $\mathbf{p}$ , whose  $j$ th element is a constant coefficient  $p_j$  describing the physical property of the  $j$ th equivalent source and approximates the function  $p(x_j, y_j, z_j)$  (equations 32 and 35) evaluated at the point  $(x_j, y_j, z_j)$ . This approximation results in a discrete version of the classical or generalized upward continuation integrals (equations 27 and 35) given by

$$d_i^p(\mathbf{p}) = \sum_{j=1}^M p_j g_{ij}, \quad (57)$$

where  $g_{ij} \equiv g(x_i - x_j, y_i - y_j, z_i - z_j)$  (equation 35) is the harmonic function representing the potential field produced, at the observation point  $(x_i, y_i, z_i)$ ,  $i = 1, \dots, N$ , by an equivalent source that is located at the point  $(x_j, y_j, z_j)$ ,  $j = 1, \dots, M$ , and has a unit (scalar) physical property.

The harmonic functions  $g_{ij}$  (equation 57) can describe the potential field produced by different kinds of equivalent sources. As pointed out before (Cordell, 1992; Guspí and Novara, 2009; Li et al., 2014), these harmonic functions are independent of the nature of the observed potential-field data and can be chosen according to the characteristics of the problem. The necessary condition is that these functions must be harmonic and vanish as the distance to the source increases. Table 1 shows the kind of equivalent-sources, the mathematical/physical meaning of the harmonic functions as well as the kind of observed potential-field data used by several authors. As shown in this table, Dampney (1969) preserves the physical relationship between the observed potential-field data and their actual sources by approximating an observed Bouguer anomaly by the vertical component of the gravitational attraction exerted by point masses. On the other hand, Cordell (1992) and Guspí and Novara (2009) release the physical relationship between the observed potential

field data and their actual sources. Specifically, Cordell (1992) approximates an observed Bouguer anomaly by the gravitational potential produced by point masses whereas Guspí and Novara (2009) approximate a total-field anomaly by the second directional derivative of a generic harmonic function representing a higher-order potential produced by point sources.

We call to attention that, depending on the definition of the harmonic functions  $g_{ij}$  (equation 57) and the geometry of the equivalent layer, the coefficients  $p_j$  may approximate a particular analytical form of the continuous physical property distribution  $p(x', y', z')$  (equation 32). Consider, for example, the particular case in which an observed total-field anomaly  $\Delta T_i^o$  (equation 8) is approximated by the potential-field  $d_i^p(\mathbf{p})$ ,  $i = 1, \dots, N$ , produced by a planar equivalent layer of dipoles located at a constant depth  $z_c$  and the harmonic functions are defined according to  $g_{ij} \equiv g(x_i - x_j, y_i - y_j, z_i - z_c)$  (equation 43). Additionally, consider that the dipoles are conveniently arranged in a uniform grid of points spaced at  $\Delta x$  and  $\Delta y$  along, respectively, the  $x$  and  $y$  directions. In this case, we have

$$d_i^p(\mathbf{p}) = \sum_{j=1}^M p_j \left( k_m \frac{\mu_0}{4\pi} \hat{\mathbf{F}}^\top \mathbf{H}_{ij} \hat{\mathbf{h}} \right), \quad (58)$$

where  $\mathbf{H}_{ij}$  is a matrix that is similar to  $\mathbf{H}_i$  (equation 45), with elements  $\partial_{\alpha\beta}\theta_{ij} \equiv \partial_{\alpha\beta}\theta(x_i - x_j, y_i - y_j, z_i - z_j)$ ,  $\alpha = x, y, z$ ,  $\beta = x, y, z$  (equation 38), the unit vectors  $\hat{\mathbf{F}}$  and  $\hat{\mathbf{h}}$  are defined in equations 43–46 and the coefficients  $p_j$  represent a magnetic moment distribution (in  $\text{Am}^2$ ) in the equivalent layer. In equation 58, the use of an arbitrary unit vector  $\hat{\mathbf{h}}$ , which corresponds to use equivalent sources with arbitrary magnetization direction, results in a parameter vector  $\mathbf{p}$  whose elements  $p_j$  have no evident physical meaning. On the other hand, by setting the unit vector  $\hat{\mathbf{h}} = \hat{\mathbf{m}}$  (equation 8), which corresponds to use equivalent sources with the same magnetization direction as the true sources, the elements  $p_j$  of the

parameter vector  $\mathbf{p}$  assume, according to equations 47–52, a particular analytical form given by

$$p_j = \frac{\Delta s m}{2\pi k_g \rho G} \delta g_j, \quad (59)$$

where  $\Delta s = \Delta x \Delta y$  and  $\delta g_j \equiv \delta g(x_j, y_j, z_c)$  (equation 1) is the gravity disturbance produced by the actual and unknown geological sources at the points  $(x_j, y_j, z_c)$ . Notice that  $p_j$  (equation 59) represents a discrete form of the continuous physical property distribution  $p(x', y', z')$  defined by equation 52.

The analytical representation of the physical property distribution in the equivalent layer (equation 52) is not only a mathematical concept without practical application; rather, it can be used in practice. For example, Li et al. (2014) cleverly took advantage of the theoretical relationship between the gravity disturbance (equation 1) and the all-positive magnetic moment distribution (equation 52) at the equivalent layer. By exploring a particular form of this theoretical relationship, they imposed a positivity constraint to estimate the magnetic moment distribution within the equivalent layer. However, in most practical applications, the numerical values of the coefficients are estimated, whatsoever the possible analytical form that they approximate.

In the geophysical literature, the technique of estimating a particular parameter vector  $\mathbf{p}$  yielding a predicted potential field  $d_i^p(\mathbf{p})$  (equation 57) that is close to the observed potential field  $d_i^o$  at the points  $(x_i, y_i, z_i)$ ,  $i = 1, \dots, N$ , is named either “equivalent source technique” or “equivalent layer technique”. Here, we opted for using the second term.

## Classical equivalent layer

The classical equivalent layer approach consists in solving a linear inverse problem to estimate the parameter vector  $\mathbf{p}$  containing the coefficients  $p_j$ ,  $j = 1, \dots, M$ , describing the physical property of the equivalent sources. Let  $\mathbf{d}^o$  be the observed data vector, whose  $i$ th element  $d_i^o$ ,  $i = 1, \dots, N$ , represents a potential-field observation at the point  $(x_i, y_i, z_i)$ . Let us also define the predicted data vector  $\mathbf{d}^p(\mathbf{p})$ , whose  $i$ th element is the predicted potential-field data  $d_i^p(\mathbf{p})$  (equation 57) at the point  $(x_i, y_i, z_i)$ . According to equation 57, the predicted data at each observation point is a linear combination of harmonic functions  $g_{ij}$  in which  $p_j$ ,  $j = 1, \dots, M$ , are the coefficients. Consequently, the predicted data vector  $\mathbf{d}^p(\mathbf{p})$  can be written in matrix notation as follows

$$\mathbf{d}^p(\mathbf{p}) = \mathbf{G}\mathbf{p}, \quad (60)$$

where  $\mathbf{G}$  is an  $N \times M$  dense matrix whose  $ij$ th element is the harmonic (Green's) function  $g_{ij}$  (equation 57).

The classical approach consists in estimating the parameter vector  $\mathbf{p}$  by solving the linear inverse problem of minimizing the difference between the observed data  $\mathbf{d}^o$  and the predicted data  $\mathbf{d}^p(\mathbf{p})$  (equation 60). To obtain a stable estimate  $\mathbf{p}^*$ , this linear inverse problem is generally constrained by using a regularization function (Tikhonov and Arsenin, 1977; Aster et al., 2005). For example, a stable estimate  $\mathbf{p}^*$  can be obtained by minimizing the goal function

$$\Gamma(\mathbf{p}) = \Psi(\mathbf{p}) + \mu\Omega(\mathbf{p}), \quad (61)$$

where the first term  $\Psi(\mathbf{p})$  is the data misfit function given by

$$\Psi(\mathbf{p}) = \|\mathbf{d}^o - \mathbf{d}^p(\mathbf{p})\|_2^2, \quad (62)$$

which is the squared Euclidean norm of the difference between the observed data  $\mathbf{d}^o$  and the predicted data  $\mathbf{d}^p(\mathbf{p})$  (equation 60), and  $\mu$  is a positive real number controlling the trade-off between the data misfit function and the zeroth-order Tikhonov regularization (Tikhonov and Arsenin, 1977; Aster et al., 2005) given by

$$\Omega(\mathbf{p}) = \|\mathbf{p}\|_2^2, \quad (63)$$

which is the squared Euclidean norm of the parameter vector  $\mathbf{p}$ . Other example of regularization function commonly used in the equivalent layer technique is the first-order Tikhonov regularization, which imposes smoothness on the estimated physical property distribution.

After obtaining an estimate  $\mathbf{p}^*$ , a desired linear transformation, such as interpolation, reduction to the pole and upward (or downward) continuation, is performed by

$$\mathbf{d}'(\mathbf{p}^*) = \mathbf{T} \mathbf{p}^*, \quad (64)$$

where  $\mathbf{d}'(\mathbf{p}^*)$  is an  $L \times 1$  vector whose  $k$ th element  $d'_k(\mathbf{p}^*)$  is the transformed-potential field at position  $(x_k, y_k, z_k)$ ,  $k = 1, \dots, L$ . We stress that the transformed potential-field data are calculated at  $L$  points  $(x_k, y_k, z_k)$ ,  $k = 1, \dots, L$ , which are not necessarily coincident with the  $N$  observation points  $(x_i, y_i, z_i)$ ,  $i = 1, \dots, N$ . Finally,  $\mathbf{T}$  is an  $L \times M$  matrix whose  $kj$ th element  $t_{kj}$  is an harmonic (Green's) function representing the desired transformed-potential field produced by the  $j$ th equivalent source with unitary physical property at the  $k$ th point  $(x_k, y_k, z_k)$ .

For example, let us return to the case in which an observed total-field anomaly  $\Delta T_i^o$  (equation 8) is approximated by the predicted potential-field  $d_i^p(\mathbf{p})$  given by equation 58. In this case, the element  $t_{kj}$  of the matrix  $\mathbf{T}$  (equation 64) used for computing the vertical derivative of the observed total-field anomaly at the observation points can be defined as

follows

$$t_{ij} = k_m \frac{\mu_0}{4\pi} \hat{\mathbf{F}}^\top \partial_z \mathbf{H}_{ij} \hat{\mathbf{h}}, \quad (65)$$

where

$$\partial_z \mathbf{H}_{ij} = \begin{bmatrix} \partial_{xxz}\theta_{ij} & \partial_{xyz}\theta_{ij} & \partial_{xzz}\theta_{ij} \\ \partial_{xyy}\theta_{ij} & \partial_{yyz}\theta_{ij} & \partial_{yzz}\theta_{ij} \\ \partial_{xzz}\theta_{ij} & \partial_{yzz}\theta_{ij} & \partial_{zzz}\theta_{ij} \end{bmatrix} \quad (66)$$

is a  $3 \times 3$  matrix whose elements  $\partial_{\alpha\beta z}\theta_{ij} \equiv \partial_{\alpha\beta z}\theta(x_i - x_j, y_i - y_j, z_i - z_c)$ ,  $\alpha = x, y, z$ ,  $\beta = x, y, z$ , are defined in equation 39. Additionally, the element  $t_{ij}$  of the matrix  $\mathbf{T}$  (equation 64) used for computing the reduced-to-the-pole anomaly (or RTP anomaly) at the observation points is given by

$$t_{ij} = k_m \frac{\mu_0}{4\pi} \partial_{zz}\theta_{ij}, \quad (67)$$

where  $\partial_{zz}\theta_{ij} \equiv \partial_{zz}\theta(x_i - x_j, y_i - y_j, z_i - z_c)$  are defined according to equation 38. We stress that this transformation requires that the equivalent sources have the same magnetization direction as the true magnetic sources, which mean that the unit vector  $\hat{\mathbf{h}}$  in equation 58 must be equal to the unit vector  $\hat{\mathbf{m}}$  in equation 8. Finally, the element  $t_{kj}$  of the matrix  $\mathbf{T}$  (equation 64) used for computing an upward-continued or interpolated total-field anomaly is given by

$$t_{kj} = k_m \frac{\mu_0}{4\pi} \hat{\mathbf{F}}^\top \mathbf{H}_{kj} \hat{\mathbf{h}}, \quad (68)$$

where  $\mathbf{H}_{kj}$  is the same matrix defined in equation 45, but with the elements  $\partial_{\alpha\beta}\theta_{kj} \equiv \partial_{\alpha\beta}\theta(x_k - x_j, y_k - y_j, z_k - z_c)$  (equation 38),  $\alpha = x, y, z$ ,  $\beta = x, y, z$ , evaluated at the continuation or interpolation points  $(x_k, y_k, z_k)$ ,  $k = 1, \dots, L$ .

## Computational aspects

Generally, the linear inverse problem of estimating a stable parameter vector  $\mathbf{p}^*$  minimizing the goal function (equation 61) deals with a large and dense matrix  $\mathbf{G}$  (equation 60). Consequently, this problem deals with large-scaled matrix computations, making the equivalent layer technique computationally inefficient. As properly pointed out by Barnes and Lumley (2011), the key to a successful application of the equivalent layer rests with carefully designed algorithm that can handle large-scaled problems efficiently and reliably. Any algorithm designed to solve problems involving large-scaled matrix computations needs to take advantage of the particular structure of these matrices instead of using strategies that were developed for general matrices. The performance of an algorithm can be increased, for example, by exploiting the fact that a symmetric matrix can be stored in half the space of a general matrix or by designing matrix-vector products that consider only the nonzero entries (Press et al., 1992; Golub and Loan, 2013). The computational efficiency of an algorithm depends, amongst other factors, on the amount of required arithmetic and storage. A way of determining the amount of required arithmetic is by counting the number of floating-point operations (*flops*), which is the number of additions, subtractions, multiplications or divisions of floating-point numbers (Boyd and Vandenberghe, 2004; Golub and Loan, 2013).

A stable estimate  $\mathbf{p}^*$  minimizing the goal function (equation 61) can be obtained, for example, by using an overdetermined formulation (Menke, 1989)

$$\mathbf{p}^* = \left( \mathbf{G}^\top \mathbf{G} + \mu \mathbf{I} \right)^{-1} \mathbf{G}^\top \mathbf{d}^o \quad (69)$$

or an underdetermined formulation

$$\mathbf{p}^* = \mathbf{G}^\top \left( \mathbf{G} \mathbf{G}^\top + \mu \mathbf{I} \right)^{-1} \mathbf{d}^o, \quad (70)$$

depending on the relative number  $M$  of parameters with respect to the number  $N$  of data. Notice that, in equation 69,  $\mathbf{I}$  is the  $M \times M$  identity matrix, whereas in equation 70,  $\mathbf{I}$  is the  $N \times N$  identity matrix. While the linear system to be solved in equation 69 contains an  $M \times M$  matrix  $(\mathbf{G}^\top \mathbf{G} + \mu \mathbf{I})$ , the one to be solved in equation 70 contains an  $N \times N$  matrix  $(\mathbf{G}\mathbf{G}^\top + \mu \mathbf{I})$ . The number of *flops* needed to construct the linear systems shown in equations 69 and 70 are, respectively,

$$f_c^o = M^2 N + M + 2MN \quad (71)$$

and

$$f_c^u = M N^2 + N + 2MN . \quad (72)$$

Here, by regarding the symmetry of the matrices involved, we consider that the solution of the linear systems are obtained from the Cholesky factorization. In this case, the number of *flops* needed to solve the linear systems shown in equations 69 and 70 are, respectively,

$$f_s^o = \frac{1}{3}M^3 + 2M^2 \quad (73)$$

and

$$f_s^u = \frac{1}{3}N^3 + 2N^2 . \quad (74)$$

Generally, the number of equivalent sources  $M$  are greater than the number of potential-field data  $N$  and, therefore, the overdetermined solution (equation 69) is more computationally expensive than the underdetermined solution (equation 70).

Several authors have developed different algorithms to improve the computational efficiency of the equivalent layer technique. Leão and Silva (1989) developed a fast method for processing a regular grid of potential-field data. The method consists in estimating an equivalent layer which exactly reproduces the potential-field data within a small data

window. The data window is shifted over the whole gridded data set in a procedure similar to a discrete convolution. The equivalent layer extends beyond the moving-data window and is located at a depth between two and six times the grid spacing of the observations. For each data window, the equivalent layer is estimated by solving an underdetermined linear system similar to that one presented in equation 70. After estimating an equivalent layer, the transformed-potential field is computed only at the center of the moving-data window. The use of a small moving-data window greatly reduces the total number of *flops* and memory storage. The computational efficiency of this method relies on the strategy of constructing the equivalent layer by successively solving small linear systems instead of solving just one large linear system for the entire equivalent layer. Based on the authors' literature reviews, one of the fastest methods known today is that one proposed by Leão and Silva (1989). Mendonça and Silva (1994) also followed the strategy of solving successive small linear systems for constructing an equivalent layer. Their method is based on the equivalent-data concept, which consists in determining a subset of all potential-field data (named equivalent-data set), such that the interpolating surface that fits the chosen subset also automatically fits all remaining data. The equivalent data set is obtained by iteratively introducing the potential-field observation with the greatest residual in the preceding iteration. By applying to the interpolation problem, the method is optimized by approximating dot products by the discrete form of an analytic integration that can be evaluated with less computational effort. According to the authors, the equivalent-data set is usually smaller than the total number of potential-field observations, leading to computational savings. The authors also pointed out that the computational efficiency of the method depends on the number of equivalent data. If the potential-field anomaly is nonsmooth, the number of equivalent data can be large and the method will be less efficient than the classical approach.

By following a different strategy, Li and Oldenburg (2010) developed a rapid method that transforms the dense matrix  $\mathbf{G}$  (equation 60) into a sparse one by using a wavelet technique. After obtaining a sparse representation of the matrix  $\mathbf{G}$ , these authors estimate the physical-property distribution within the equivalent layer by using an overdetermined formulation similar to that one shown in equation 69. These authors pointed out that, given the sparse representation, their method reduces the computational time required for solving the linear system by as many as two orders of magnitude if compared with the same formulation using a dense matrix. Barnes and Lumley (2011) followed a similar strategy and transformed the dense matrix  $\mathbf{G}$  (equation 60) into a sparse one. However, differently from Li and Oldenburg (2010), their method operates in the space domain by grouping equivalent sources far from an observation point into blocks with average physical property. This procedure aims at reducing the memory storage and achieving computational efficiency by solving the transformed linear system with a weighted-least-squares conjugate-gradient algorithm. Notice that, instead of constructing the equivalent layer by solving successive small linear systems, these last two methods first transform the large linear system into a sparse one and then take advantage of this sparseness.

Oliveira Jr. et al. (2013) developed a fast method based on the reparameterization of the physical-property distribution within the equivalent layer. These authors divided the equivalent layer into a regular grid of equivalent-source windows inside which the physical-property distribution is described by bivariate polynomial functions. By using this polynomial representation, the inverse problem of constructing the equivalent layer is posed in the space of the total number of polynomial coefficients within all equivalent-source windows instead of in the space of the total number of equivalent sources. According to Oliveira Jr. et al. (2013), the computational efficiency of their method relies on the fact that the to-

tal number of polynomial coefficients needed to describe the physical property distribution within the equivalent layer is generally much smaller than the number of equivalent sources, leading to a very smaller linear system to be solved. These authors could verify that the total number of *flops* needed for building and solving the linear inverse problem of estimating the total number of polynomial coefficients can be reduced by as many as three and four orders of magnitude, respectively, if compared with the same inverse problem of estimating the physical property of each equivalent source forming the equivalent layer.

The method presented by Cordell (1992) and after generalized by Guspí and Novara (2009) does not estimate the physical property distribution within the equivalent layer by solving a linear system. The physical property of the sources, which are located below each potential-field data, are iteratively updated by a procedure that removes the maximum residual between the observed and predicted data. The total number of *flops* required by these iterative methods for estimating the physical-property distribution within the equivalent layer depends on the total number of iterations, however this number is generally much smaller than the total number of *flops* required to solve a large-scaled linear system. Generally, the most computational expensive step in each iteration of these methods is the forward problem of calculating the potential-field data produced by the equivalent layer.

## APPLICATIONS

We present numerical tests to validate the theoretical magnetic-moment distribution within a planar equivalent layer (equations 52 and 59) and also demonstrate the power of the equivalent layer technique in processing potential-field data. In all tests, we place an equivalent source beneath each data point. The synthetic data used in all tests are produced by two rectangular prisms with density  $1000 \text{ kg/m}^3$  and total magnetization with intensity

10 A/m, inclination  $30^\circ$  and declination  $-10^\circ$  (Figure 3). The smaller prism has the top at 0.05 km and side lengths equal to 2 km, 2 km and 1.95 km along, respectively, the  $x$ -,  $y$ - and  $z$ -axis. The greater prism has the top at 0.1 km and side lengths equal to 2 km, 6 km and 2 km along the  $x$ -,  $y$ - and  $z$ -axis, respectively. In almost all tests, the synthetic data produced by the simulated prisms and the equivalent layers are calculated on the undulating surface shown in Figure 4; The exceptions will be specified in the text. Finally, the simulated local-geomagnetic field in all tests has a constant direction with inclination  $6^\circ$  and declination  $-40.5^\circ$ .

### Validation of the theoretical magnetic-moment distribution

We compare the total-field anomaly  $\Delta T_i^o$  (equation 8) and RTP anomaly  $\Delta T_i^P$  (equation 9) produced by the simulated prisms (Figures 5a and 5b) with the total-field anomaly and RTP anomaly produced by a planar equivalent layer (Figures 5b and 5e) of dipoles located at a constant depth  $z_c = -200$  m. These anomalies are calculated on a regular grid of  $90 \times 90$  points  $(x_i, y_i, z_i)$ ,  $i = 1, \dots, N = 8100$ , which are regularly spaced at  $\approx 337$  m along the horizontal directions  $x$  and  $y$ .

The total-field anomaly produced by the equivalent layer (Figure 5c) is calculated by using equation 58, where the coefficients  $p_j$ ,  $j = 1, \dots, N = 8100$ , describing the physical property of each dipole are calculated by using the discrete form of the theoretical magnetic-moment distribution (equation 59). Notice that, in this case, the coefficients  $p_j$  are not estimated by solving any linear inverse problem. Rather, they are directly calculated by equation 59. The RTP anomaly produced by the planar equivalent layer (Figures 5d) is calculated by using equation 64, where the elements  $t_{ij}$  of the matrix  $\mathbf{T}$  are defined by

equation 67.

The differences between the total-field and RTP anomalies produced by the simulated prisms (Figures 5a and 5b) and the equivalent layer (Figures 5c and 5d), calculated at the same points, are shown in Figures 5e and 5f. Notice that the differences are very close to zero over the entire area, except at the borders, where they reach the maxima absolute values. The maxima absolute differences between the total-field and RTP anomalies are, respectively,  $\approx 5$  nT and  $\approx 5.6$  nT. These small differences, therefore, validate the theoretical magnetic-moment distribution defined by equation 59.

Figure 6a shows the physical property distribution within the equivalent layer, which is calculated by using the discrete form of the theoretical magnetic-moment distribution (equation 59). Figure 6b shows the synthetic gravity disturbance (equation 1) used in equation 59 for calculating the magnetic-moment distribution shown in Figure 6a. Notice that the physical property distribution within the equivalent layer (Figure 6a) is all positive, which is in accordance with our mathematical analysis.

These results validate the theoretical premise that a planar equivalent layer of dipoles having a magnetic-moment distribution defined by equation 59 is able to reproduce a discrete set of total-field anomaly data as well as retrieve the true RTP anomaly. Consequently, despite the numerical approximations, these results also validate the continuous theoretical magnetic-moment distribution given by equation 52.

## **Estimation of the magnetic moment distribution**

We present two numerical tests very similar to that presented in the previous subsection. The only difference is that the magnetic-moment distribution within the equivalent layer is

estimated by solving a linear inverse problem.

In the first test, the unit vector  $\hat{\mathbf{h}}$  (equation 58) defining the magnetization direction of the equivalent sources is equal to the unit vector  $\hat{\mathbf{m}}$  (equation 8) defining the magnetization direction of the simulated prisms (Figure 3). Figure 7a shows the estimated magnetic-moment distribution within the planar equivalent layer as defined in the previous test. Figure 7b shows the difference between the estimated magnetic-moment (Figure 7a) and the theoretical magnetic-moment distribution (Figure 6a). We observe null differences over almost the entire layer. The maxima absolute differences are  $\approx 0.06 \times 10^9 \text{ Am}^2$  and occur at the borders.

The total-field and RTP anomalies predicted by the planar equivalent layer are shown in Figures 8a and 8b, respectively. These anomalies are calculated by using equations 58, 64 and 67 with the estimated magnetic-moment distribution shown in Figure 7a. The differences between the total-field and RTP anomalies produced by the simulated prisms (Figures 5a and 5b) and by the equivalent layer (Figures 8a and 8b), calculated at the same points, are shown in Figures 8c and 8d, respectively. As we can see, they are very close to zero over the entire area. The maxima absolute differences between the total-field and RTP anomalies are, respectively,  $\approx 0.02 \text{ nT}$  and  $\approx 226.84 \text{ nT}$ . They occur along well-defined striations that are closely aligned with the declination of the simulated local-geomagnetic field ( $-40.5^\circ$ ). The presence of these artefacts has been already pointed out by Li et al. (2014). They observed these striations by applying the equivalent-layer to perform the RTP in the space domain. According to their analysis, they suggest that these striations are caused by the inherent instabilities of the RTP transformation at low latitudes. They showed, for purely induced magnetic sources, that these striations can occur even in cases where the estimated physical property distribution within the equivalent layer is regularized.

In spite of these striations, Figures 8c and 8d show that the equivalent layer is able to closely retrieve the total-field and RTP anomalies produced by the simulated prisms.

In the second test, we use a unit vector  $\hat{\mathbf{h}}$  (equation 58) having the same direction as the local-geomagnetic field (inclination  $6^\circ$  and declination  $-40.5^\circ$ ). Notice that, in this case, the equivalent sources have a magnetization direction which is different from that of the true sources (inclination  $30^\circ$  and declination  $-10^\circ$ ). Figure 9a shows the estimated magnetic-moment distribution within the planar equivalent layer defined previously. It is apparent that this estimated magnetic-moment distribution is very different from either the theoretical (Figure 6a) or estimated (Figure 7a) magnetic-moment distributions obtained in the previous tests.

The total-field and RTP anomalies produced by this planar equivalent layer are shown in Figures 9b and 9c, respectively. As in the previous tests, these anomalies are calculated by using equations 58, 64 and 67. Notice that this equivalent layer with magnetization direction different from that of the true sources is able to retrieve the total-field anomaly produced by the simulated prisms (Figure 5a). The maxima absolute differences are  $\approx 18$  nT. On the other hand, this equivalent layer is not able to retrieve the correct RTP anomaly (Figure 5b). This result confirms the well-known fact that, for calculating the RTP anomaly, it is necessary to know the magnetization direction of the true sources. Although this equivalent layer cannot be used to calculate the RTP anomaly, it can be used to perform other transformations like upward continuation, for example, which does not require the use of the magnetization direction of the true sources. Figure 9d shows the true noise-free total-field anomaly produced by the simulated prisms (Figure 3) at the same horizontal coordinates of the original data (Figure 5a) on a horizontal plane at  $z = -1400$  m. Figure 9e shows the upward-continued total-field anomaly computed on the horizontal plane

at  $z = -1400$  m by using the planar equivalent layer with the estimated magnetic-moment distribution shown in Figure 9a. Figure 9f shows the difference between the total-field anomalies shown in Figures 9d and 9e. As we can see, even with a magnetization direction which is different from that of the true magnetic sources, the equivalent layer reproduces the total-field anomaly produced by the true sources at the continuation plane. The maxima absolute differences are 74 nT, but they are located at a corner of the area.

These tests show that, by using equivalent sources with the same magnetization direction as the true magnetic sources, we obtain a magnetic-moment distribution (Figure 7a) very close to the theoretical magnetic-moment distribution which is shown in Figure 6a and calculated with equation 59. On the other hand, if the magnetization direction of the equivalent sources is different from that of the true magnetic sources, the estimated magnetic-moment distribution within the equivalent (Figure 9a) layer is different from the theoretical magnetic-moment distribution. Moreover, this estimated magnetic-moment distribution (Figure 9a) does not recover the correct RTP anomaly. These results confirm that the theoretical magnetic-moment distribution can only be estimated if the equivalent sources have the same magnetization direction of the true magnetic sources.

### **The use of alternative equivalent sources and harmonic functions**

In the previous tests, we have used a planar equivalent layer of dipoles for approximating the total-field anomaly produced by the simulated prisms (Figure 3). In those tests, we use harmonic functions  $g_{ij}$  (equation 57) representing the total-field anomaly produced by dipoles (equation 43) and the predicted data is calculated by equation 58. Consequently, the coefficients  $p_j$  (equation 57) represent the magnetic-moment distribution within the equivalent

layer. Here, we also estimate the physical property distribution within an equivalent layer to fit the total-field anomaly produced by the simulated prisms (Figure 3). However, the tests presented in this section differ from the previous ones in several aspects. Figures 10a and 11a show, respectively, the coordinates (black points)  $(x_i, y_i, z_i)$ ,  $i = 1, \dots, N = 3600$ , and the noise-corrupted total-field anomaly produced by the simulated prisms at these coordinates. The total-field anomaly is contaminated with a Gaussian noise having null mean and standard deviation of 5 nT. The coordinates (black points in Figure 10a) are located on a regular grid of  $120 \times 30$  points separated by  $\approx 252.1$  m and  $\approx 1034.5$  m intervals along, respectively, the  $x$  and  $y$  directions.

Differently from the previous tests, the equivalent sources are located in an undulating surface (Figure 10b). The biggest difference, however, is that we use the harmonic functions  $g_{ij}$  (equation 57) defined by equation 37, with  $\alpha = z$ . Notice that, in this case, the harmonic functions describe the vertical component of the gravitational attraction produced by point masses and the coefficients  $p_j$  (equation 57),  $j = 1, \dots, N = 3600$ , do not represent the magnetic-moment distribution within the equivalent layer. In fact, they have no evident physical meaning.

After solving a linear inverse problem to estimate the coefficients  $p_j$  (not shown) defined within the undulating equivalent layer, we calculated the predicted total-field anomaly (Figure 11b) at the coordinates shown in Figure 10a. As we can see in the histogram of the residuals (Figure 11c) defined as the difference between the total-field anomalies shown in Figures 11a and 11b, the estimated mean  $\mu$  is very close to zero and the standard deviation approximates that one of the Gaussian noise (5 nT), showing that the equivalent layer yields a very good data fit.

Although this equivalent layer cannot be used for calculating the RTP anomaly, it can be used for calculating other transformations. In this test, we calculate the total-gradient amplitude of the total-field anomaly by using equation 64. This quantity is commonly used in applied geophysics to determine the horizontal limits of the magnetic sources. It is defined as the squared root of the sum of the squared first spatial derivatives of the potential-field data. Because in this test we used the harmonic functions  $g_{ij}$  (equation 57) defined by equation 37 with  $\alpha = z$ , we calculate the first spatial derivatives of the total-field anomaly by using equation 38 with a fixed  $\beta = z$ . To calculate the spatial derivatives of the total-field anomaly data along the  $x$ ,  $y$ , and  $z$  axes, we used  $\alpha = x$ ,  $y$ , and  $z$ , respectively. Figures 11d and 11e show, respectively, the total-gradient amplitude produced by the simulated prisms and the undulating equivalent layer. These data were calculated at the coordinates (black points) shown in Figure 10a and their differences are shown in Figure 11f. As we can see, the differences are very close to zero throughout the area.

Notice that, in this test, the harmonic functions  $g_{ij}$  (equation 57) describe the vertical component of the gravitational attraction produced by points masses. Such harmonic functions are commonly used in applications of the equivalent layer technique to process gravity data. In this test, however, we use such harmonic functions for processing total-field anomaly data. As we have already pointed out, this approach is perfectly possible from the mathematical point of view because the total-field anomaly data are approximated by a linear combination of harmonic functions. The results presented in this test show the versatility of the equivalent layer technique in processing total-field anomaly data.

## COMPUTATIONAL REPRODUCIBILITY

All numerical tests presented here are implemented in the freely usable and distributable Python programming language. Our implementation relies on the open-source libraries `numpy` and `scipy` (Jones et al., 2001; Walt et al., 2011, <http://scipy.org>) for array-based computations, `matplotlib` (Hunter, 2007, <http://matplotlib.org>) for plots and maps, and `Fatiando a Terra` (Uieda et al., 2013, <http://www.fatiando.org>) for geophysical modelling and inversion. The computational experiments were performed in Jupyter (formerly IPython) notebooks (Pérez and Granger, 2007, <http://jupyter.org>). The notebook files combine the source code, the results and figures generated by the code and rich text to explain the analysis. All source code, Jupyter notebooks, synthetic data, and results can be found at the online repository <https://github.com/pinga-lab/Review-eqlayer>. **(Note to reviewers: the online repository will be made public upon publication).**

## SUMMARY

The mathematical base of equivalent layer technique dates back to around the 19th century. However, it was not used in geophysics until the second half of the 20th century to process and to interpret potential-field data. Due to its high computational demand, the equivalent layer technique has only raised moderate interest of geophysicists. In the beginning, the technique was greatly explored for processing potential-field data with a limited number of observations. Next, by following different approaches, the computational aspects of the equivalent layer technique were improved to make feasible its application for processing large data sets. Surprisingly, since the first applications of the equivalent layer technique, its theoretical aspects have received little attention. Theoretical aspects of the estimated

physical property distribution within the equivalent layer, for example, has only been addressed recently. Specifically, some studies have determined the relationship between an all-positive magnetic-moment distribution within a continuous and planar equivalent layer and the pseudogravity anomaly produced by the true sources on the plane defining the equivalent layer. This relationship, however, was determined by considering that the magnetic sources are magnetized by induction and the observations are located on a horizontal plane.

We present, in the space domain, a sound generalization of this theoretical relationship between the magnetic-moment distribution within a planar equivalent layer and the gravity data. This generalization allows us to prove that the all-positive magnetic-moment distribution exists even if the magnetization direction of the true sources is different from that of the local-geomagnetic field. Moreover, our approach neither requires magnetic sources with constant magnetization intensity nor observations located on a horizontal plane. We have shown that the all-positive magnetic-moment distribution within a planar equivalent layer can be estimated if the equivalent sources have the same magnetization direction of the true magnetic sources whether it is aligned with the local-geomagnetic field or not.

Currently, the equivalent layer technique is mostly used to process potential-field data. However, we call attention that it has also been employed indirectly in interpretation. This occurs, for example, if the desired transformation of the potential-field data requires the knowledge of the magnetization direction of the true sources, as in the reduction to the pole. If the interpreter does not know the magnetization direction of the true sources, the reduction to the pole fails. In this case, different hypotheses about the magnetization direction of the sources can be tried to estimate a sound reduced-to-the-pole data. Once calculated a sound reduction to the pole, not only the transformed potential-field, but

also the magnetic-moment distribution within the planar equivalent layer are concentrated directly over the true sources. Consequently, not only the reduced-to-the-pole data, but also the magnetic-moment distribution within the planar equivalent layer can be used to determine the horizontal location of the true sources.

It is expected that, in the future, the equivalent layer technique will be widely used not only for processing but also for interpreting potential-field data. Independently of the applications of the equivalent layer technique, the challenge now is to improve its computational efficiency, making it feasible to deal with large potential-field data sets.

## REFERENCES

- Aster, R. C., B. Borchers, and C. H. Thurber, 2005, Parameter estimation and inverse problems (international geophysics): Academic Press.
- Baranov, V., 1957, A new method for interpretation of aeromagnetic maps: Pseudo-gravimetric anomalies: *Geophysics*, **22**, 359–382.
- Barnes, G., 2012, Interpolating the gravity field using full tensor gradient measurements: *First Break*, **30**, 97–101.
- , 2014, Reconstructing the gravity gradient anomaly field from surveys with wide line spacing using equivalent source processing: an error analysis: *Geophysical Prospecting*, **62**, 646–657.
- Barnes, G., and J. Lumley, 2011, Processing gravity gradient data: *GEOPHYSICS*, **76**, I33–I47.
- Baumann, H., E. Klingelé, and I. Marson, 2012, Absolute airborne gravimetry: a feasibility study: *Geophysical Prospecting*, **60**, 361–372.
- Bhattacharyya, B. K., 1967, Some general properties of potential fields in space and frequency domain: a review: *Geoexploration*, **5**, 127–143.
- Bhattacharyya, B. K., and K. C. Chan, 1977, Reduction of magnetic and gravity data on an arbitrary surface acquired in a region of high topographic relief: *Geophysics*, **42**, 1411–1430.
- Blakely, R. J., 1996, *Potential theory in gravity and magnetic applications*: Cambridge University Press.
- Boggs, D., and M. Dransfield, 2004, Analysis of errors in gravity derived from the falcon airborne gravity gradiometer: ASEG-PESA Airborne Gravity 2004 Workshop, *Geoscience Australia Record*, 135–141.

- Bott, M. H. P., 1967, Solution of the linear inverse problem in magnetic interpretation with application to oceanic magnetic anomalies: *Geophysical Journal of the Royal Astronomical Society*, **13**, 313–323.
- Bott, M. H. P., and A. Ingles, 1972, Matrix methods for joint interpretation of two-dimensional gravity and magnetic anomalies with application to the iceland-faeroe ridge: *Geophysical Journal of the Royal Astronomical Society*, **30**, 55–67.
- Boyd, S., and L. Vandenberghe, 2004, *Convex optimization*: Cambridge University Press.
- Chandler, V. W., J. S. Koski, W. J. Hinze, and L. W. Braile, 1981, Analysis of multi-source gravity and magnetic anomaly data sets by movingwindow application of poissons theorem: *GEOPHYSICS*, **46**, 30–39.
- Cordell, L., 1992, A scattered equivalent-source method for interpolation and gridding of potential-field data in three dimensions: *GEOPHYSICS*, **57**, 629–636.
- Cordell, L., and P. T. Taylor, 1971, Investigation of magnetization and density of a north atlantic seamount using poissons theorem: *GEOPHYSICS*, **36**, 919–937.
- Dampney, C. N. G., 1969, The equivalent source technique: *GEOPHYSICS*, **34**, 39–53.
- Daneš, Z. F., 1962, Structure calculations from gravity data and density logs: *Transactions of the Society of Mining Engineers of AIME*, **223**, 23–29.
- Davis, K., and Y. Li, 2011, Fast solution of geophysical inversion using adaptive mesh, space-filling curves and wavelet compression: *Geophysical Journal International*, **185**, 157–166.
- Emilia, D. A., 1973, Equivalent sources used as an analytic base for processing total magnetic field profiles: *GEOPHYSICS*, **38**, 339–348.
- Garland, G. D., 1951, Combined analysis of gravity and magnetic anomalies: *GEOPHYSICS*, **16**, 51–62.

- Glennie, C. L., K. P. Schwarz, A. M. Bruton, R. Forsberg, A. V. Olesen, and K. Keller, 2000, A comparison of stable platform and strapdown airborne gravity: *Journal of Geodesy*, **74**, 383–389.
- Goldstein, H., C. P. Poole Jr., and J. L. Safko, 1980, *Classical mechanics*, 3 ed.: Addison-Wesley.
- Golub, G. H., and C. F. V. Loan, 2013, *Matrix computations* (Johns Hopkins studies in the mathematical sciences): Johns Hopkins University Press.
- Gunn, P. J., 1975, Linear transformations of gravity and magnetic fields: *Geophysical Prospecting*, **23**, 300–312.
- Guspí, F., A. Introcaso, and B. Introcaso, 2004, Gravity-enhanced representation of measured geoid undulations using equivalent sources: *Geophysical Journal International*, **159**, 1–8.
- Guspí, F., and I. Novara, 2009, Reduction to the pole and transformations of scattered magnetic data using newtonian equivalent sources: *GEOPHYSICS*, **74**, L67–L73.
- Hammer, S., 1945, Estimating ore masses in gravity prospecting: *GEOPHYSICS*, **10**, 50–62.
- Hansen, R. O., and Y. Miyazaki, 1984, Continuation of potential fields between arbitrary surfaces: *GEOPHYSICS*, **49**, 787–795.
- Henderson, R. G., 1960, A comprehensive system of automatic computation in magnetic and gravity interpretation: *GEOPHYSICS*, **25**, 569–585.
- , 1970, On the validity of the use of the upward continuation integral for total magnetic intensity data: *GEOPHYSICS*, **35**, 916–919.
- Henderson, R. G., and I. Zietz, 1949, The upward continuation of anomalies in total magnetic intensity fields: *GEOPHYSICS*, **14**, 517–534.

- Hofmann-Wellenhof, B., and H. Moritz, 2005, *Physical geodesy*: Springer.
- Hulot, G., T. Sabaka, N. Olsen, and A. Fournier, 2015, 5.02 - the present and future geomagnetic field, *in* *Treatise on Geophysics*, second edition ed.: Elsevier, 33–78.
- Hunter, J. D., 2007, Matplotlib: A 2d graphics environment: *Computing in Science & Engineering*, **9**, 90–95.
- Jeffreys, H., and B. Jeffreys, 2000, *Methods of mathematical physics*, 3ed. ed.: Cambridge University Press. Cambridge Mathematical Library.
- Jones, E., T. Oliphant, P. Peterson, et al., 2001, SciPy: Open source scientific tools for Python. ([Online; accessed 2016-09-22]).
- Kellogg, O. D., 1929, *Foundations of potential theory*: Frederick Ungar Publishing Company.
- LaFehr, T. R., 1965, The estimation of the total amount of anomalous mass by gauss's theorem: *Journal of Geophysical Research*, **70**, 1911–1919.
- Lane, R., 2004, Integrating ground and airborne data into regional gravity compilation: ASEG-PESA Airborne Gravity 2004 Workshop, *Geoscience Australia Record*, 81–97.
- Langel, R. A., and W. J. Hinze, 1998, *The magnetic field of the earth's lithosphere: The satellite perspective*: Cambridge University Press.
- Leão, J. W. D., and J. B. C. Silva, 1989, Discrete linear transformations of potential field data: *GEOPHYSICS*, **54**, 497–507.
- Li, Y., M. Nabighian, and D. W. Oldenburg, 2014, Using an equivalent source with positivity for low-latitude reduction to the pole without striation: *GEOPHYSICS*, **79**, J81–J90.
- Li, Y., and D. W. Oldenburg, 2010, Rapid construction of equivalent sources using wavelets: *GEOPHYSICS*, **75**, L51–L59.
- MacLennan, K., and Y. Li, 2013, Denoising multicomponent csem data with equivalent

- source processing techniques: *Geophysics*, **78**, E125–E135.
- Martinez, C., and Y. Li, 2016, Denoising of gravity gradient data using an equivalent source technique: *GEOPHYSICS*, **81**, G67–G79.
- Mayhew, M. A., 1982, Application of satellite magnetic anomaly data to curie isotherm mapping: *Journal of Geophysical Research: Solid Earth*, **87**, 4846–4854.
- Mendonça, C. A., 1992, Interpolação de dados de campo potencial através da camada equivalente: PhD thesis, Universidade Federal do Pará, Belém do Pará, Brazil.
- , 2004, Automatic determination of the magnetization density ratio and magnetization inclination from the joint interpretation of 2d gravity and magnetic anomalies: *GEOPHYSICS*, **69**, 938–948.
- Mendonça, C. A., and J. B. C. Silva, 1994, The equivalent data concept applied to the interpolation of potential field data: *GEOPHYSICS*, **59**, 722–732.
- Menke, W., 1989, *Geophysical data analysis: Discrete inverse theory*: Academic Press, Inc.
- Nabighian, M. N., M. E. Ander, V. J. S. Grauch, R. O. Hansen, T. R. LaFehr, Y. Li, W. C. Pearson, J. W. Peirce, J. D. Phillips, and M. E. Ruder, 2005a, Historical development of the gravity method in exploration: *GEOPHYSICS*, **70**, 63ND–89ND.
- Nabighian, M. N., V. J. S. Grauch, R. O. Hansen, T. R. LaFehr, Y. Li, J. W. Peirce, J. D. Phillips, and M. E. Ruder, 2005b, The historical development of the magnetic method in exploration: *GEOPHYSICS*, **70**, 33ND–61ND.
- Oliveira Jr., V. C., V. C. F. Barbosa, and L. Uieda, 2013, Polynomial equivalent layer: *GEOPHYSICS*, **78**, G1–G13.
- Pawlowski, R. S., 1994, Greens equivalent-layer concept in gravity bandpass filter design: *GEOPHYSICS*, **59**, 69–76.
- Pedersen, L. B., 1991, Relations between potential fields and some equivalent sources: *GEO-*

- PHYSICS, **56**, 961–971.
- Pérez, F., and B. E. Granger, 2007, IPython: A System for Interactive Scientific Computing: Computing in Science & Engineering, **9**, 21–29.
- Pilkington, M., and W. E. S. Urquhart, 1990, Reduction of potential field data to a horizontal plane: GEOPHYSICS, **55**, 549–555.
- Press, W. H., B. P. Flannery, S. A. Teukolsky, and W. T. Vetterling, 1992, Numerical recipes in c: The art of scientific computing, second edition: Cambridge University Press.
- Roy, A., 1962, Ambiguity in geophysical interpretation: GEOPHYSICS, **27**, 90–99.
- Silva, J. B. C., 1986, Reduction to the pole as an inverse problem and its application to low-latitude anomalies: GEOPHYSICS, **51**, 369–382.
- Silva, J. B. C., and G. W. Hohmann, 1984, Airborne magnetic susceptibility mapping: Exploration Geophysics, **15**, 1–13.
- Skeels, D. C., 1947, Ambiguity in gravity interpretation: GEOPHYSICS, **12**, 43–56.
- Tikhonov, A. N., and V. Y. Arsenin, 1977, Solutions of ill-posed problems: V. H. Winston & Sons.
- Twomey, S., 1977, Introduction to the mathematics of inversion in remote sensing and indirect measurements: Dover Publications, Inc.
- Uieda, L., V. C. Oliveira Jr., and V. C. F. Barbosa, 2013, Modeling the earth with fatiando a terra: Proceedings of the 12th Python in Science Conference, 96 – 103.
- Vaníček, P., and E. J. Krakiwsky, 1987, Geodesy: The concepts, second edition: Elsevier Science.
- Von Frese, R. R. B., W. J. Hinze, and L. W. Braile, 1981, Spherical earth gravity and magnetic anomaly analysis by equivalent point source inversion: Earth and Planetary Science Letters, **53**, 69 – 83.

- Walt, S., S. C. Colbert, and G. Varoquaux, 2011, The numpy array: A structure for efficient numerical computation: *Computing in Science & Engineering*, **13**, 22–30.
- Whittaker, E. T., 2012, *A history of the theories of aether and electricity: From the age of descartes to the close of the nineteenth century (classic reprint)*: Forgotten Books.
- Xia, J., and D. R. Sprowl, 1991, Correction of topographic distortion in gravity data: *GEOPHYSICS*, **56**, 537–541.
- Xia, J., D. R. Sprowl, and D. Adkins-Heljeson, 1993, Correction of topographic distortions in potential-field data; a fast and accurate approach: *GEOPHYSICS*, **58**, 515–523.
- Zidarov, D., 1965, Solution of some inverse problems of applied geophysics: *Geophysical Prospecting*, **13**, 240–246.

## LIST OF FIGURES

1 2D representation of a 3D regular region with volume  $v$  and boundary defined by a regular surface  $S$ , whose outward normal is represented by  $\hat{\mathbf{n}}$ .  $x_i$ ,  $y_i$  and  $z_i$  are the coordinates of a point located within  $v$ . These coordinates are referred to a Cartesian system with the  $x$  axis pointing into the page, the  $y$  axis pointing to right and the  $z$  axis pointing downward.

2 2D representation of a 3D regular region with volume  $v$  and boundary defined by the union of a hemisphere  $S_1$  with radius  $R$  and a horizontal plane  $S_2$  at the vertical coordinate  $z = z_c$ .  $\hat{\mathbf{n}}_1$  and  $\hat{\mathbf{n}}_2$  represent, respectively, the normal to the surfaces  $S_1$  and  $S_2$ . The points  $(x_i, y_i, z_i)$  and  $(x_i, y_i, z_s)$  are located, respectively, inside and outside  $v$ . These points are located at the same distance from the horizontal plane  $S_2$ , so that  $z_i = z_c - \Delta z$  and  $z_s = z_c + \Delta z$ . The coordinates are referred to a Cartesian system with the  $x$  axis pointing into the page, the  $y$  axis pointing to right and the  $z$  axis pointing downward.

3 Synthetic bodies with constant density  $\rho = 1000 \text{ kg/m}^3$  and constant magnetization vector with intensity  $m = 10 \text{ A/m}$ , inclination  $30^\circ$  and declination  $-10^\circ$ . The geomagnetic field has inclination  $6^\circ$  and declination  $-40.5^\circ$ .

4 Undulating observation surface (grayscale) where we calculate the synthetic data produced by the simulated prisms (Figure 3). The white rectangles represent the horizontal projection of the simulated prisms.

5 (a) Noise-free total-field (equation 8) and (b) RTP (equation 9) anomalies produced by the synthetic prisms (Figure 3) on the undulating surface shown in Figure 4. (c) Total-field and (d) RTP anomalies produced by the planar equivalent layer which is defined in Figure 6. The magnetic moment distribution of this equivalent layer was directly calculated by equation 59 and is shown in Figure 6a. (e) Difference between the total-field anomalies shown in c and a. (f) Difference between the RTP anomalies shown in d and b. These anomalies are calculated at a regular grid of  $90 \times 90$  points located on the observation surface (Figure 4). The black rectangles represent the horizontal projection of the simulated prisms (Figure 3). The field values are in nT.

6 (a) Theoretical magnetic-moment distribution (equation 59) calculated within a planar equivalent layer. The layer is formed by a regular grid of  $90 \times 90$  dipoles located at coordinates  $(x_j, y_j, z_c)$ ,  $j = 1, \dots, N = 8100$ , where  $z_c = -200 \text{ m}$ . This magnetic-moment distribution is calculated by using (b) the noise-free gravity disturbance (equation 1), which is produced by the synthetic prisms (Figure 3) at the coordinates of the dipoles. The black rectangles represent the horizontal projection of the simulated prisms (Figure 3).

7 (a) Estimated magnetic-moment distribution within the planar equivalent layer. The estimate was obtained by solving a linear inverse problem subject to fitting the noise-free total-field anomaly shown in Figure 5a. The equivalent sources have the same magnetization direction as the simulated prisms (Figure 3). (b) Difference between the estimated magnetic-moment distribution shown in a and the theoretical magnetic-moment distribution (Figure 6a). The black rectangles represent the horizontal projection of the simulated prisms (Figure 3).

8 (a) Total-field and (b) RTP anomalies produced by the planar equivalent layer whose estimated magnetic moment distribution is shown in Figure 7a. (c) Difference between the total-field anomalies shown in a and Figure 5a. (d) Difference between the RTP anomalies shown in b and Figure 5b. These anomalies were calculated at a regular grid of  $90 \times 90$  points located on the undulating surface (Figure 4). The black rectangles represent the horizontal projection of the simulated prisms (Figure 3). The field values are in nT.

9 (a) Estimated magnetic-moment distribution (in  $10^9 \text{ Am}^2$ ) within the planar equivalent layer. The estimate was obtained by solving a linear inverse problem subject to fitting the noise-free total-field anomaly shown in Figure 5a. The equivalent sources have the same magnetization direction as the local-geomagnetic field (inclination  $6^\circ$  and declination  $-40.5^\circ$ ), which is different from the magnetization direction of the simulated prisms (Figure 3). (b) Total-field and (c) RTP anomalies (in nT) produced by the planar equivalent layer whose estimated magnetic moment distribution is shown in a. (d) True and (e) upward-continued noise-free total-field anomaly computed on a horizontal plane at  $z = -1400 \text{ m}$ . The true anomaly shown in d was produced by the simulated prisms (Figure 3). The upward-continued anomaly shown in e was predicted by the planar equivalent layer having the estimated magnetic-moment distribution shown in a. (f) Difference between the total-field anomalies shown in e and d. All data are calculated at a regular grid of  $90 \times 90$  points. The black rectangles represent the horizontal projection of the simulated prisms (Figure 3).

10 (a) Undulating observation surface where we calculate the total-field anomaly (Figure 11a) and the total-gradient amplitude (Figure 11d) produced by the simulated prisms (Figure 3). These magnetic data are calculated at a regular grid of  $120 \times 30$  points (black dots) in the  $x$  and  $y$  directions. (b) Undulating surface (grayscale) defining an uneven equivalent layer. The white rectangles represent the horizontal projection of the simulated prisms (Figure 3).

11 (a) Total-field anomaly produced by the simulated prisms (Figure 3) and contaminated with a Gaussian noise having null mean and standard deviation equal to 5 nT. (b) Total-field anomaly produced by the equivalent layer defined on the undulating surface shown in Figure 10b. Both data are given in nT. (c) Histogram of the residuals defined as the difference between the total-field anomalies shown in b and a. The black-dashed line represent a best fit Gaussian curve. The estimated mean and standard deviation are represented by  $\mu$  and  $\sigma$ , respectively. (d) True total-gradient amplitude (noise-free) produced by the simulated prisms (Figure 3). (e) Total-gradient amplitude produced by the equivalent layer defined on the uneven surface shown in Figure 10b. Both data are given in nT/m. (f) Difference between the total-gradient amplitudes shown in e and d. All data are calculated at a regular grid of  $120 \times 30$  points represented as black dots in Figure 10a. The black rectangles represent the horizontal projection of the simulated prisms (Figure 3).

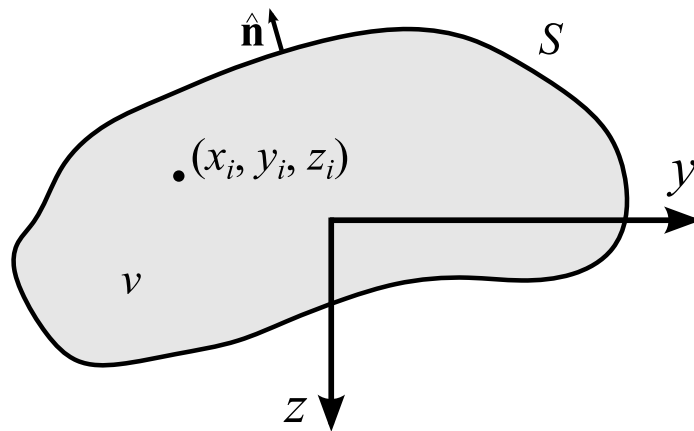


Figure 1: 2D representation of a 3D regular region with volume  $v$  and boundary defined by a regular surface  $S$ , whose outward normal is represented by  $\hat{\mathbf{n}}$ .  $x_i$ ,  $y_i$  and  $z_i$  are the coordinates of a point located within  $v$ . These coordinates are referred to a Cartesian system with the  $x$  axis pointing into the page, the  $y$  axis pointing to right and the  $z$  axis pointing downward.

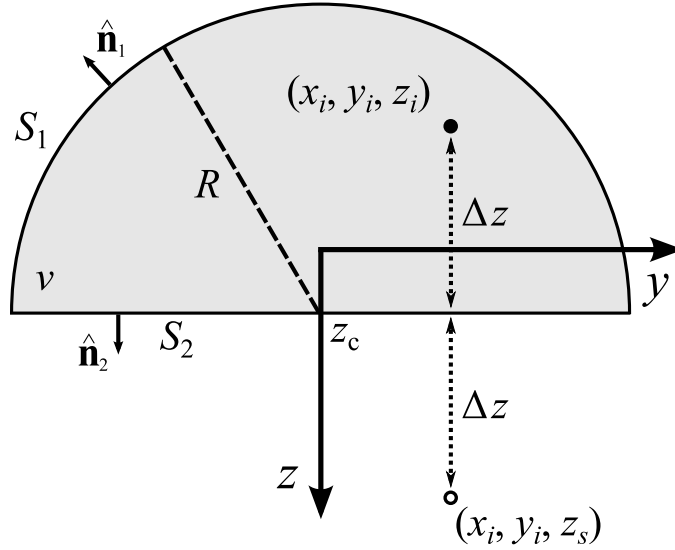


Figure 2: 2D representation of a 3D regular region with volume  $v$  and boundary defined by the union of a hemisphere  $S_1$  with radius  $R$  and a horizontal plane  $S_2$  at the vertical coordinate  $z = z_c$ .  $\hat{\mathbf{n}}_1$  and  $\hat{\mathbf{n}}_2$  represent, respectively, the normal to the surfaces  $S_1$  and  $S_2$ . The points  $(x_i, y_i, z_i)$  and  $(x_i, y_i, z_s)$  are located, respectively, inside and outside  $v$ . These points are located at the same distance from the horizontal plane  $S_2$ , so that  $z_i = z_c - \Delta z$  and  $z_s = z_c + \Delta z$ . The coordinates are referred to a Cartesian system with the  $x$  axis pointing into the page, the  $y$  axis pointing to right and the  $z$  axis pointing downward.

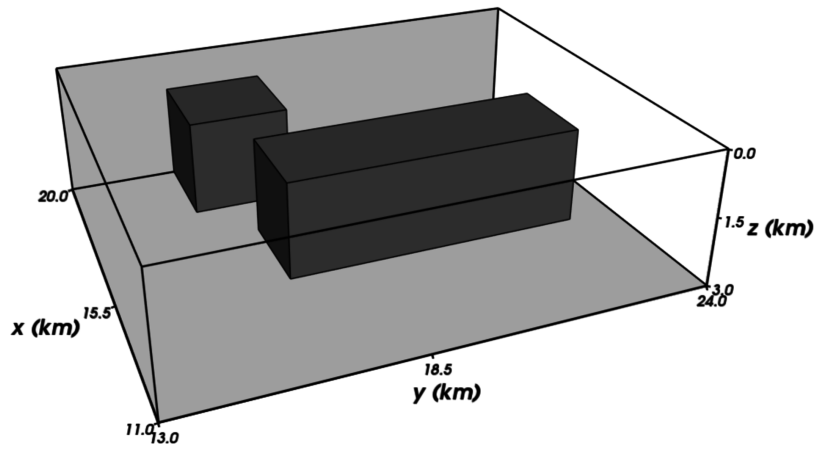


Figure 3: Synthetic bodies with constant density  $\rho = 1000 \text{ kg/m}^3$  and constant magnetization vector with intensity  $m = 10 \text{ A/m}$ , inclination  $30^\circ$  and declination  $-10^\circ$ . The geomagnetic field has inclination  $6^\circ$  and declination  $-40.5^\circ$ .

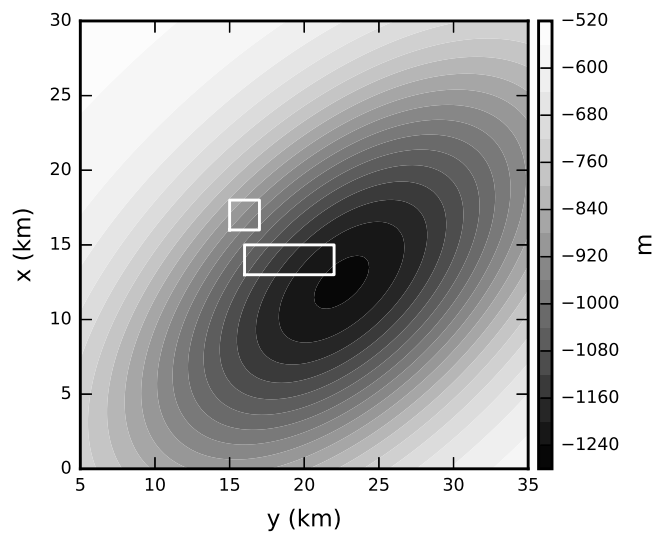


Figure 4: Undulating observation surface (grayscale) where we calculate the synthetic data produced by the simulated prisms (Figure 3). The white rectangles represent the horizontal projection of the simulated prisms.

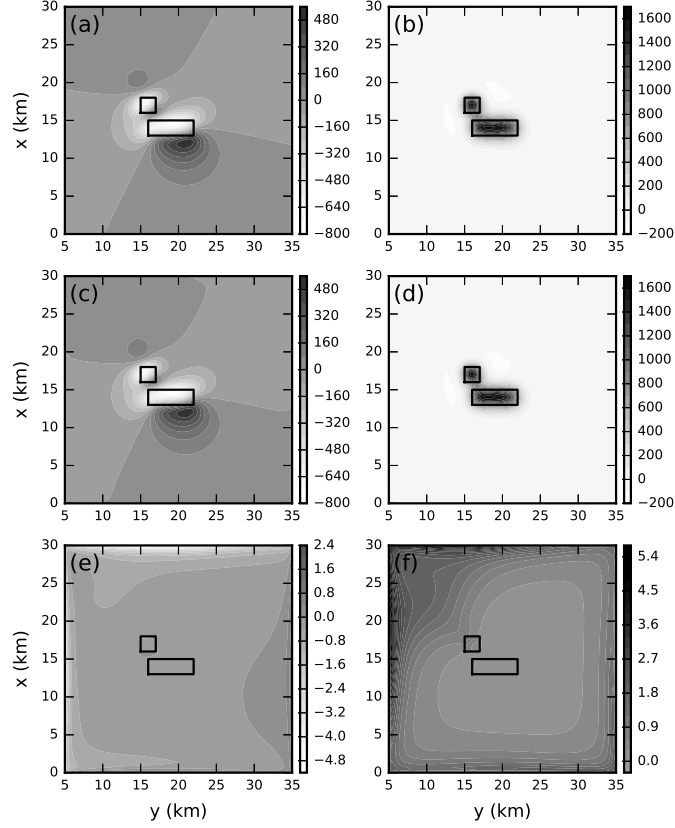


Figure 5: (a) Noise-free total-field (equation 8) and (b) RTP (equation 9) anomalies produced by the synthetic prisms (Figure 3) on the undulating surface shown in Figure 4. (c) Total-field and (d) RTP anomalies produced by the planar equivalent layer which is defined in Figure 6. The magnetic moment distribution of this equivalent layer was directly calculated by equation 59 and is shown in Figure 6a. (e) Difference between the total-field anomalies shown in c and a. (f) Difference between the RTP anomalies shown in d and b. These anomalies are calculated at a regular grid of  $90 \times 90$  points located on the observation surface (Figure 4). The black rectangles represent the horizontal projection of the simulated prisms (Figure 3). The field values are in nT.

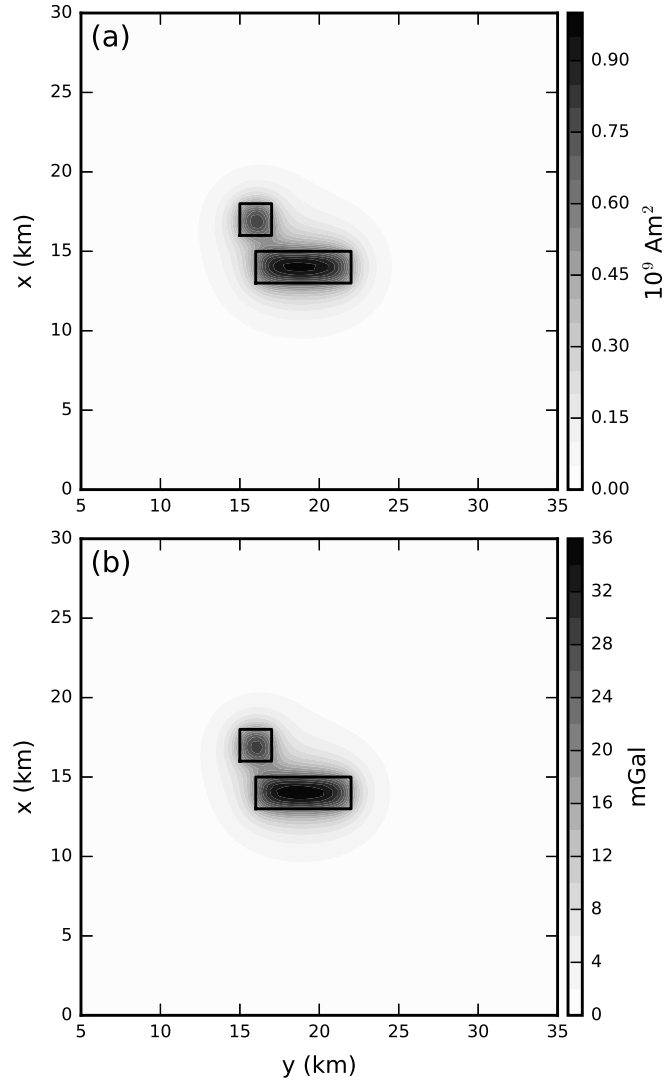


Figure 6: (a) Theoretical magnetic-moment distribution (equation 59) calculated within a planar equivalent layer. The layer is formed by a regular grid of  $90 \times 90$  dipoles located at coordinates  $(x_j, y_j, z_c)$ ,  $j = 1, \dots, N = 8100$ , where  $z_c = -200$  m. This magnetic-moment distribution is calculated by using (b) the noise-free gravity disturbance (equation 1), which is produced by the synthetic prisms (Figure 3) at the coordinates of the dipoles. The black rectangles represent the horizontal projection of the simulated prisms (Figure 3).

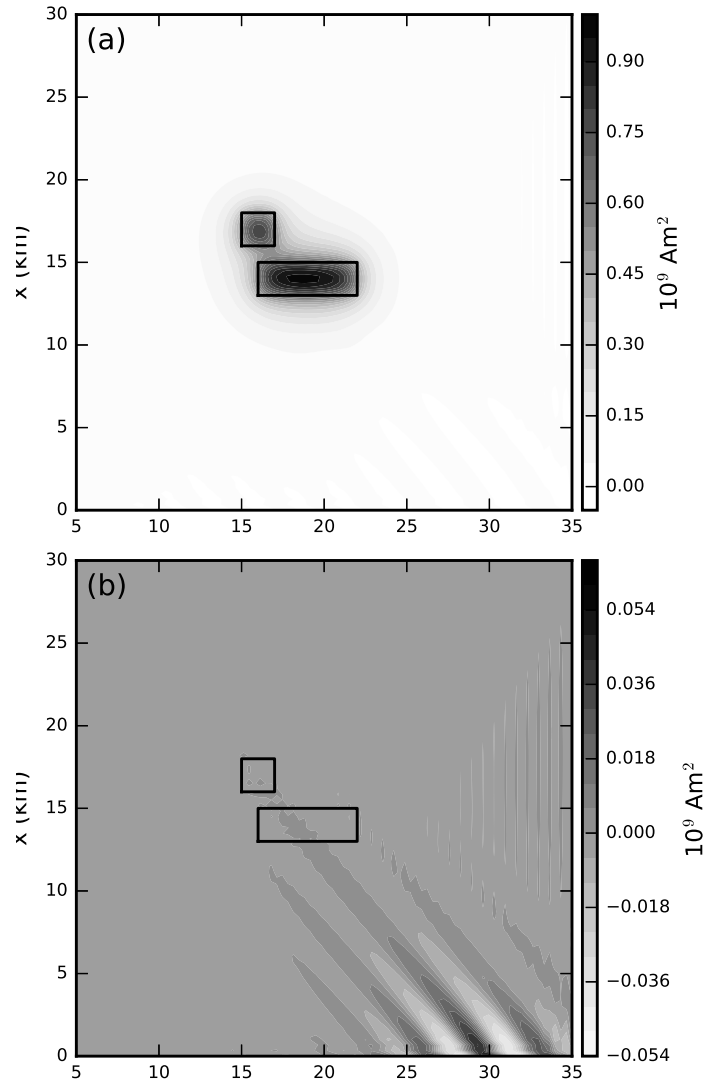


Figure 7: (a) Estimated magnetic-moment distribution within the planar equivalent layer. The estimate was obtained by solving a linear inverse problem subject to fitting the noise-free total-field anomaly shown in Figure 5a. The equivalent sources have the same magnetization direction as the simulated prisms (Figure 3). (b) Difference between the estimated magnetic-moment distribution shown in a and the theoretical magnetic-moment distribution (Figure 6a). The black rectangles represent the horizontal projection of the simulated prisms (Figure 3).

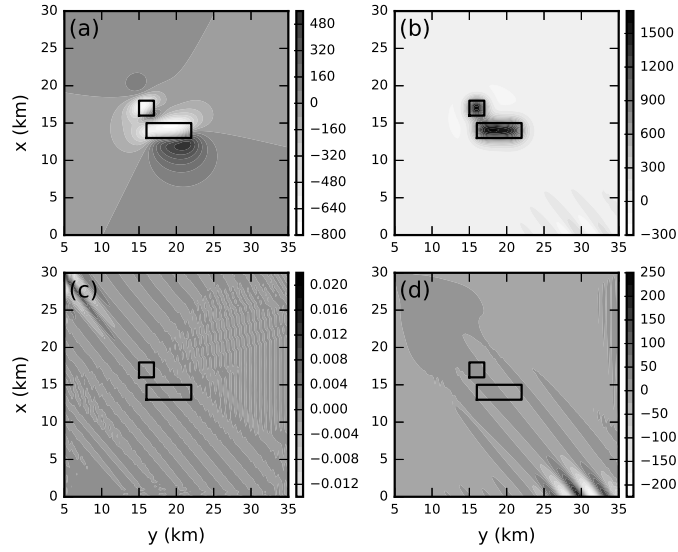


Figure 8: (a) Total-field and (b) RTP anomalies produced by the planar equivalent layer whose estimated magnetic moment distribution is shown in Figure 7a. (c) Difference between the total-field anomalies shown in a and Figure 5a. (d) Difference between the RTP anomalies shown in b and Figure 5b. These anomalies were calculated at a regular grid of  $90 \times 90$  points located on the undulating surface (Figure 4). The black rectangles represent the horizontal projection of the simulated prisms (Figure 3). The field values are in nT.

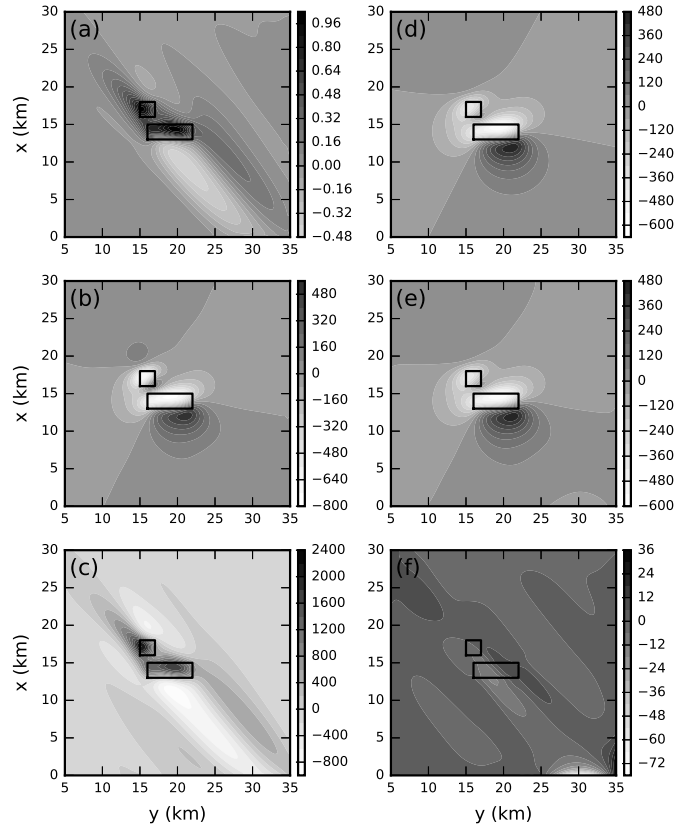


Figure 9: (a) Estimated magnetic-moment distribution (in  $10^9 \text{ Am}^2$ ) within the planar equivalent layer. The estimate was obtained by solving a linear inverse problem subject to fitting the noise-free total-field anomaly shown in Figure 5a. The equivalent sources have the same magnetization direction as the local-geomagnetic field (inclination  $6^\circ$  and declination  $-40.5^\circ$ ), which is different from the magnetization direction of the simulated prisms (Figure 3). (b) Total-field and (c) RTP anomalies (in nT) produced by the planar equivalent layer whose estimated magnetic moment distribution is shown in a. (d) True and (e) upward-continued noise-free total-field anomaly computed on a horizontal plane at  $z = -1400 \text{ m}$ . The true anomaly shown in d was produced by the simulated prisms (Figure 3). The upward-continued anomaly shown in e was predicted by the planar equivalent layer having the estimated magnetic-moment distribution shown in a. (f) Difference between the total-field anomalies shown in e and d. All data are calculated at a regular grid of  $90 \times 90$  points. The black rectangles represent the horizontal projection of the simulated prisms (Figure 3).

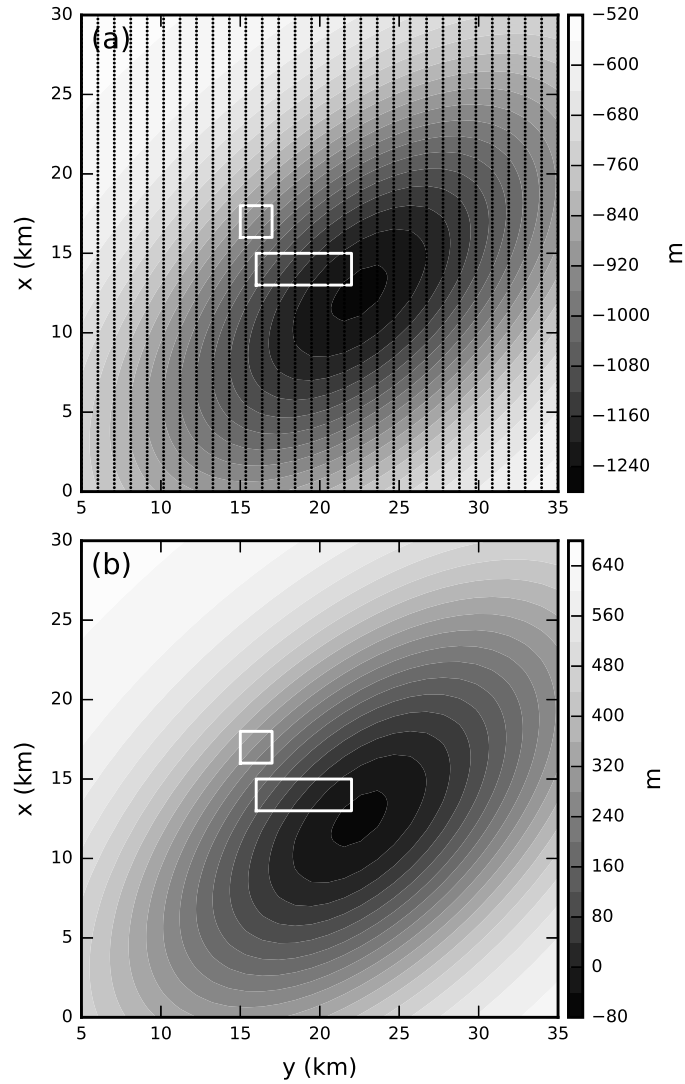


Figure 10: (a) Undulating observation surface where we calculate the total-field anomaly (Figure 11a) and the total-gradient amplitude (Figure 11d) produced by the simulated prisms (Figure 3). These magnetic data are calculated at a regular grid of  $120 \times 30$  points (black dots) in the  $x$  and  $y$  directions. (b) Undulating surface (grayscale) defining an uneven equivalent layer. The white rectangles represent the horizontal projection of the simulated prisms (Figure 3).

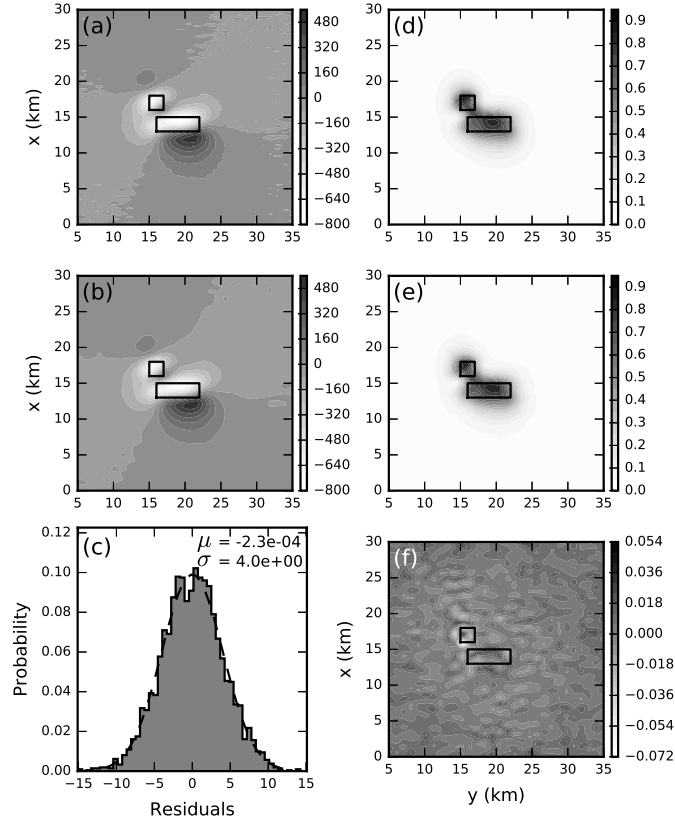


Figure 11: (a) Total-field anomaly produced by the simulated prisms (Figure 3) and contaminated with a Gaussian noise having null mean and standard deviation equal to 5 nT. (b) Total-field anomaly produced by the equivalent layer defined on the undulating surface shown in Figure 10b. Both data are given in nT. (c) Histogram of the residuals defined as the difference between the total-field anomalies shown in b and a. The black-dashed line represent a best fit Gaussian curve. The estimated mean and standard deviation are represented by  $\mu$  and  $\sigma$ , respectively. (d) True total-gradient amplitude (noise-free) produced by the simulated prisms (Figure 3). (e) Total-gradient amplitude produced by the equivalent layer defined on the uneven surface shown in Figure 10b. Both data are given in nT/m. (f) Difference between the total-gradient amplitudes shown in e and d. All data are calculated at a regular grid of  $120 \times 30$  points represented as black dots in Figure 10a. The black rectangles represent the horizontal projection of the simulated prisms (Figure 3).

## LIST OF TABLES

- 1 Observed potential-field data and the mathematical/physical meaning of the harmonic functions  $g_{ij}$  (equation 57) describing the potential field produced by the equivalent sources used by several authors.

<b>Author(s)</b>	<b>Equivalent sources</b>	<b>Harmonic function <math>g_{ij}</math></b>	<b>Observed data</b>
Dampney (1969)	point masses	vertical component of the gravitational attraction	Bouguer anomaly
Emilia (1973)	lines of dipoles	total-field anomaly	total-field anomaly
Hansen and Miyazaki (1984)	uniformly-magnetized plane faces	magnetic scalar potential	total-field anomaly
Silva (1986)	doublets	total-field anomaly	total-field anomaly
Cordell (1992)	point masses	gravitational potential	Bouguer anomaly
Guspí and Novara (2009)	generic point sources producing a higher-order potential	second-directional derivative of the higher-order potential	total-field anomaly
Barnes and Lumley (2011)	rectangular prisms	second derivatives of the gravitational potential	gravity gradient
Oliveira Jr. et al. (2013)	dipoles	total-field anomaly	total-field anomaly
Li et al. (2014)	rectangular prisms	total-field anomaly	total-field anomaly

Table 1: Observed potential-field data and the mathematical/physical meaning of the harmonic functions  $g_{ij}$  (equation 57) describing the potential field produced by the equivalent sources used by several authors.